Neurocomputing 462 (2021) 14–30

Contents lists available at ScienceDirect

Neurocomputing

journal homepage: www.elsevier.com/locate/neucom

fMRI-SI-STBF: An fMRI-informed Bayesian electromagnetic spatio-temporal extended source imaging

Ke Liu [a], Zhu Liang Yu [b,c,*], Wei Wu [b,c,*], Xun Chen [d], Zhenghui Gu [b,c], Cuntai Guan [e]

[a] Chongqing Key Laboratory of Computational Intelligence, Chongqing University of Posts and Telecommunications, Chongqing 400065, China
[b] College of Automation Science and Engineering, South China University of Technology, Guangzhou 510641, China
[c] Pazhou Lab., Guangzhou 510330, China
[d] Department of Electronic Engineering and Information Science, University of Science and Technology of China, Hefei 230026, China
[e] School of Computer Science and Engineering, Nanyang Technological University 639798, Singapore

ARTICLE INFO

Article history:
Received 22 June 2020
Revised 23 May 2021
Accepted 21 June 2021
Available online 24 June 2021
Communicated by Zidong Wang

Keywords:
EEG source imaging
fMRI priors
Empirical Bayesian
Matrix decomposition

ABSTRACT

Multimodal functional neuroimaging by integrating functional magnetic resonance imaging (fMRI) and electroencephalography (EEG) has the promise of recovering brain activities with high spatiotemporal resolution, which is crucial for neuroscience research and clinical diagnosis. However, the misalignment of the localizations between fMRI and EEG activities may degrade the accuracy of the fMRI-constrained EEG source imaging (ESI) technique. To leverage the complementary spatiotemporal resolution of fMRI and EEG in a data-driven fashion, we propose an asymmetric approach for EEG/fMRI fusion, termed fMRI-informed source imaging based on spatiotemporal basis functions (fMRI-SI-STBF). fMRI-SI-STBF employs the covariance components (CCs) derived from clusters defined by fMRI and EEG signals as spatial priors within the empirical Bayesian framework. Additionally, fMRI-SI-STBF represents the current source matrix as a linear combination of several unknown temporal basis functions (TBFs) by matrix decomposition. The relative contribution of each of the fMRI-informed and EEG-informed CCs, as well as the number and profiles of the TBFs, are all automatically determined based on the EEG data using variational Bayesian inference. Our results demonstrate that fMRI-SI-STBF can effectively utilize valid fMRI information for ESI and is robust to invalid fMRI priors. This robustness is essential for practical ESI since the validity of fMRI priors is often unclear considering that fMRI is an indirect measure of neural activity. Moreover, fMRI-SI-STBF can achieve performance improvement by incorporating temporal constraints compared to methods that use spatial constraints only. For the numerical simulations, fMRI-SI-STBF reconstructs the source extents, locations and time courses more accurately than existing EEG-fMRI ESI methods (i.e., fwMNE, fMRI-SI-SBF) and ESI methods without fMRI priors (i.e., wMNE, LORETA, SBL, SI-STBF, SI-SBF), indicated by the smaller spatial dispersion (average SD < 5 mm), distance of localization error (average DLE < 2 mm), shape error (average SE < 0.9) and larger model evidence values.

1. Introduction

Artificial intelligence has shown great achievements in brain function research [1–3], disease (e.g., COVID-19, gastric cancer) diagnosis and detection [4–6], economic growth forecast [7]. Among these applications, electromagnetic source imaging, which employs machine learning techniques to map brain cortical activities, is very important for neuroscience research and clinical diagnosis. Electroencephalography (EEG) and functional magnetic resonance imaging (fMRI) are two widely-used types of neural signals to reconstruct cortical activities. EEG records scalp electrical signals generated by the synchronized neural electrical activity of the cortex, with excellent temporal resolution (approximately milliseconds) [3,8]. However, due to volume conduction, the spatial resolution of EEG is limited. fMRI measures changes in blood oxygen level dependent (BOLD) signals at a high spatial resolution (approximately millimeters). However, the temporal resolution of fMRI is relatively poor because of the slow hemodynamic responses. Due to the complementary characteristics, it is possible to obtain a high spatiotemporal resolution mapping of cortical activities by the integration of EEG and fMRI information. Many simulations and experimental studies have demonstrated the feasibility of combining EEG and fMRI signals to obtain brain activities with high spatial and temporal resolution [3,9,10].

* Corresponding authors.
E-mail addresses: zlyu@scut.edu.cn (Z.L. Yu), auweiwu@scut.edu.cn (W. Wu).

https://doi.org/10.1016/j.neucom.2021.06.066
0925-2312/

In this work, we focus on the fMRI-informed EEG source imaging (ESI) method, which applies fMRI information to the EEG inverse problem to improve the spatial resolution of source imaging. There are two main challenges for fMRI-informed ESI: (1) How can the ESI problem be solved? (2) How can fMRI information be applied to the EEG inverse problem?

Since the number of current sources largely outnumbers the number of EEG sensors, the EEG inverse problem is heavily underdetermined, and nonunique solutions exist. To solve the inverse problem, prior constraints or regularization operators are necessary to narrow the solution space. A common solver is the L_2-norm-based method, which includes the minimum-norm estimate (MNE) [11] and its variants, such as the weighted MNE (wMNE) [3], standard low-resolution electromagnetic tomography (sLORETA) [12], and low-resolution electromagnetic tomography (LORETA) [13]. Although the L_2-norm based methods are computationally efficient, these solutions are too diffuse and usually spread over multiple cortical sulci and gyri [3,14]. To improve the spatial resolution, methods based on the L_p-norm ($p \leqslant 1$) regularizer [15] and empirical Bayesian framework (also known as sparse Bayesian learning (SBL)) [16,17] have been further developed to achieve sparse solutions. These sparse constrained methods localize cortical activities with several point sources, largely reducing the diffusion of the estimations by L_2-norm based methods.

Both experimental and clinical results have shown that scalp EEG signals are generated by neural activity to a considerable extent [18–20]. For neuroscience research and clinical diagnosis, estimating the extent of cortical activities is very important. However, the aforementioned methods provide little information on the source extent. To reconstruct extended sources, several algorithms estimate the source locations and extents by reconstructing the sparseness in the transform domains [21,22], such as the variation domain or wavelet domain. Spatial basis functions, such as spatial Gaussian functions and cortical patch bases [23], have also been used to estimate extended sources. Other studies use covariance bases derived from cortical clustering and the Green function to reconstruct extended sources [24]. The use of transform sparseness and spatial basis functions has helped to significantly improve the estimations of the extended sources.

Due to their high temporal resolution, EEG signals contain abundant temporal information. To exploit the temporal correlation structures of EEG signals, in recent years, spatiotemporal constraints have been employed to further improve the performance of the EEG inverse problem [25,26,14,27,28]. For example, some studies have used the multivariate autoregressive (MVAR) model to represent the spatiotemporal relationship among neighboring dipoles [25,29–31]. Other methods employ temporal basis functions (TBFs), which have been developed into data-independent (e.g., the Fourier dictionary and Gabor atoms) [26,32,33] or data-dependent (e.g., singular value decomposition (SVD) analysis of EEG signals) methods [34] to model the temporal smoothness of current sources. These studies show the effectiveness of temporal constraints in further improving the performance of reconstructing cortical activities. However, these TBFs were typically determined before solving the inverse problem. Accurately determining the types and number of TBFs remains an issue, and the final estimations may inherit the bias of the predefined TBFs. To remedy this problem, in our recent work [27], we proposed SI-STBF (**S**ource **I**maging based on **S**patio-**T**emporal **B**asis **F**unctions), which solves the inverse problem based on matrix factorization under the empirical Bayesian framework. According to variational Bayesian inference, SI-STBF simultaneously estimates the current sources and unknown TBFs in a data-driven manner.

To use the complementary information of EEG and fMRI, several studies have attempted to apply fMRI information to the EEG inverse problem to improve the spatial accuracy. The method that is often used for fMRI-informed ESI is the fMRI-weighted minimum-norm estimate (fwMNE) algorithm [35]. The fwMNE imposes the fMRI information in a "hard" manner, which uses the information of the statistic parameter map (SPM) derived from fMRI to constrain the spatial locations of the candidate sources of EEG. Although fwMNE has been shown to improve the spatial accuracy in many situations, it may pose some problems for cases that involve deep sources where neural activities are weakly represented in EEG signals, or rapid and transient shifts of cortical sources where cerebral blood flow caused by activated neurons cannot be detected by fMRI. Hence, many studies have imposed fMRI information in a "soft" manner [9,10,36]. For example, some studies have formulated each fMRI active cluster or network as a separate spatial prior under the parametric empirical Bayesian (PEB) framework, and have constructed the covariance components (CCs) of all clusters or networks using the Green function [9,37,38,10]. Each cluster or network has different contributions to ESI. Then Bayesian model evidence maximization is utilized to automatically adjust the relative weights of each cluster or network, which has proven to be very powerful to emphasize valid fMRI priors that are critical for generating EEG signals [9,10].

Motivated by previous studies [9,37], this paper develops an fMRI-informed ESI method based on SI-STBF, which is termed fMRI-informed source imaging based on spatiotemporal basis functions (fMRI-SI-STBF). fMRI-SI-STBF benefits from the flexible framework of SI-STBF, which can utilize various spatial priors from multiple neuroimaging modalities. For the temporal constraint, fMRI-SI-STBF represents the current source as a linear combination of several unknown TBFs using the notion of matrix decomposition. For the spatial constraint, fMRI-SI-STBF utilizes the information from both fMRI and EEG. Specifically, fMRI-SI-STBF employs spatial CCs to encode our prior knowledge of brain activity under the PEB framework. Each CC is constructed based on cortical clustering and Green's function. fMRI-SI-STBF employs both EEG-informed clusters, which are derived by data-driven parcelization (DDP) as in [27,24], and fMRI-informed clusters, which are indicated by the SPM results. The main difference between our method and previous fMRI-informed ESI methods under the PEB framework [9,10] is the utilization of source matrix factorization which incorporates both spatial and temporal constraints. According to variational Bayesian inference, the number and profiles of TBFs, and the relative contribution of each spatial prior from fMRI and EEG are all automatically determined by the EEG signals. The aim of fMRI-SI-STBF is to obtain accurate spatiotemporal estimations by combining high temporal resolution information from EEG and high spatial resolution from fMRI.

Numerical simulations and experimental data analyses were performed to evaluate the performance of the proposed method. In our simulations, we tested the influence of "valid" and "invalid" fMRI priors on the inverse solutions. In the analysis of the publicly available face processing dataset [39], the source estimates of the differential event-related potential (ERP) between faces and scrambled faces were determined and compared with the benchmark algorithms.

In summary, the contributions of this paper are twofold:

(1) An fMRI-informed ESI method with spatiotemporal constraints is proposed, which is based on source matrix factorization under the empirical Bayesian framework.
(2) Knowledge of fMRI activation and EEG recordings was encoded with spatial covariance components (CCs). Using an ARD prior, the proposed method can select the fMRI-informed and EEG-informed CCs that are related to brain activities in an automatic fashion.

The remainder of this paper is structured as follows. In Section 2, we briefly recall SI-STBF [27] and present the fMRI-SI-STBF procedure. In Section 3, we present the details for numerical simulations and validation metrics. Section 4 presents the results with both simulated and experimental EEG datasets, followed by the discussion in Section 5.

2. Method

2.1. EEG source imaging based on source matrix decomposition

The forward model for ESI can be approximated by a linear equation [1,40]:

$$\boldsymbol{B} = \boldsymbol{L}\boldsymbol{S} + \boldsymbol{\epsilon} \tag{1}$$

where $\boldsymbol{B} \in \mathbb{R}^{N_b \times N_t}$ is the EEG recordings with N_b sensors on N_t time samples. $\boldsymbol{L} \in \mathbb{R}^{N_b \times N_s}$ is the known lead-field matrix; $\boldsymbol{S} \in \mathbb{R}^{N_s \times N_t}$ denotes the unknown source activities for N_s dipoles; $\boldsymbol{\epsilon} \in \mathbb{R}^{N_b \times N_t}$ is the sensor noise, and each column follows the Gaussian distribution $\mathcal{N}(\boldsymbol{0}, \boldsymbol{\Sigma}_\epsilon)$. Without loss of generality, as in [27,34,14], we assume that the measurement equation has been whitened, i.e., $\boldsymbol{\Sigma}_\epsilon = \boldsymbol{I}$. In this work, we focus on the source model where the orientation of each dipole is perpendicular to the cortical surface.

To reconstruct brain activities, we employed the framework of the SI-STBF algorithm developed in our recent work [27] for source imaging. To incorporate the prior knowledge that cortical activities are globally sparse and locally smooth for a specific cognitive task [41,19], SI-STBF represented the source matrix $\boldsymbol{S}$ as a linear combination of multiple unknown TBFs through matrix factorization under the empirical Bayesian framework:

$$\boldsymbol{S} = \boldsymbol{W}\Phi = \sum_{k=1}^{K} \boldsymbol{w}_k \phi_k, \tag{2}$$

where $\boldsymbol{\Phi} \in \mathbb{R}^{K \times N_t}$ denotes the K unknown TBFs, which are learned from the EEG data; $\phi_k \in \mathbb{R}^{1 \times N_t}$ is the kth row of $\boldsymbol{\Phi}$ (the kth TBF); $\boldsymbol{W} \in \mathbb{R}^{N_s \times K}$ is the coding matrix describing the contribution of each TBF to the cortical sources; and $\boldsymbol{w}_k \in \mathbb{R}^{N_s \times 1}$ is the kth column of $\boldsymbol{W}$.

The priors of $\boldsymbol{\Phi}$ and $\boldsymbol{W}$ are empirically chosen as follows:

$$\begin{aligned} p(\boldsymbol{\Phi}|\boldsymbol{\alpha}) &= \prod_t \mathcal{N}(\boldsymbol{\varphi}_t|\boldsymbol{0}, \mathrm{diag}(\boldsymbol{\alpha}^{-1})) \\ p(\boldsymbol{W}|\boldsymbol{\gamma}) &= \prod_k p(\boldsymbol{w}_k|\boldsymbol{\gamma}) = \prod_k \mathcal{N}(\boldsymbol{w}_k|\boldsymbol{0}, \boldsymbol{\Sigma}_w), \boldsymbol{\Sigma}_w = \sum_{i=1}^{d_\gamma} \gamma_i^{-1} \boldsymbol{C}_i \end{aligned} \tag{3}$$

where $\boldsymbol{\varphi}_t \in \mathbb{R}^{K \times 1}$ is the tth column of $\boldsymbol{\Phi}$ and $\boldsymbol{\alpha}^{-1} = \left[\alpha_1^{-1}, \ldots, \alpha_K^{-1}\right]^\top$ is a vector of K nonnegative hyperparameters that control the relative contribution of each TBF. The prior covariance of each column of the coding matrix is a mixture of d_γ predefined CCs $\boldsymbol{C}_i$. The contribution of each CC is parameterized by the d_γ nonnegative hyperparameters $\boldsymbol{\gamma} = \left[\gamma_1, \ldots, \gamma_{d_\gamma}\right]$. Each $\boldsymbol{C}_i$ encodes a specific spatial pattern of source activities. Detailed procedures to construct $\boldsymbol{C}_i$ are presented in Section 2.2.

To facilitate the optimization of γ_i for arbitrary $\boldsymbol{C}_i$, SI-STBF makes use of the following decomposition [27,16]:

$$\boldsymbol{W} = \sum_{i=1}^{d_\gamma} \boldsymbol{A}_{[i]} \boldsymbol{\Theta}_{[i]} = \boldsymbol{A}\Theta, \tag{4}$$

where $\boldsymbol{A}_{[i]} \in \mathbb{R}^{N_s \times r_i}$ was obtained by the Cholesky decomposition such that $\boldsymbol{A}_{[i]}\boldsymbol{A}_{[i]}^\top = \boldsymbol{C}_i, r_i = \mathrm{rank}(\boldsymbol{C}_i)$. $\boldsymbol{A} = \left[\boldsymbol{A}_{[1]}, \ldots, \boldsymbol{A}_{[d_\gamma]}\right] \in \mathbb{R}^{N_s \times \sum_i r_i}, \boldsymbol{\Theta} = \left[\boldsymbol{\Theta}_{[1]}^\top, \ldots, \boldsymbol{\Theta}_{[d_\gamma]}^\top{}^\top\right] \in \mathbb{R}^{\sum_i r_i \times K}$, and $\boldsymbol{\Theta}_{[i]} \in \mathbb{R}^{r_i \times K}$. According to the decomposition in (4), the prior of $\boldsymbol{\Theta}$ is $p(\boldsymbol{\Theta}_{[i]}|\boldsymbol{\gamma}_i) \propto \exp\left(-\frac{\gamma_i}{2}\|\Theta_{[i]}\|_{\mathscr{F}}^2\right)$ [27,16]. Hence, $p(\boldsymbol{\Theta}|\boldsymbol{\gamma}) = \prod_k \mathcal{N}(\boldsymbol{\theta}_k|\boldsymbol{0}, \boldsymbol{\Sigma}^{-1})$, where $\boldsymbol{\Sigma}$ is a diagonal, $\boldsymbol{\gamma}$-dependent matrix and $\mathrm{diag}(\boldsymbol{\Sigma}) = \left[\underbrace{\gamma_1, \ldots, \gamma_1}_{r_1}, \ldots, \underbrace{\gamma_{d_\gamma}, \ldots, \gamma_{d_\gamma}}_{r_{d_\gamma}}\right]^\top$.

Combining (4) and (2) yields

$$\boldsymbol{S} = \boldsymbol{A}\Theta\Phi, \tag{5}$$

which represents the cortical source $\boldsymbol{S}$ as a linear combination of several spatial and temporal basis functions, with $\boldsymbol{A}$ being the spatial basis functions. Hence, the EEG forward problem can be expressed as

$$\boldsymbol{B} = \boldsymbol{L}\boldsymbol{A}\Theta\Phi + \boldsymbol{\varepsilon} = \boldsymbol{F}\Theta\Phi + \boldsymbol{\varepsilon}, \tag{6}$$

where $\boldsymbol{F} = \boldsymbol{L}\boldsymbol{A} = \left[\boldsymbol{F}_{[1]}, \ldots, \boldsymbol{F}_{[d_\gamma]}\right]$ and $\boldsymbol{F}_{[i]} = \boldsymbol{L}\boldsymbol{A}_{[i]} \in \mathbb{R}^{N_b \times r_i}$. $\boldsymbol{F}$ represents a modified forward model mapping cortical regions of interest (groups of dipoles clustered by the spatial basis functions $\boldsymbol{A}$) to the sensors.

In light of (6), the full probabilistic model of SI-STBF is as follows:

$$\begin{aligned} p(\boldsymbol{B}|\boldsymbol{\Theta}, \boldsymbol{\Phi}) &\propto \exp\left(-\tfrac{1}{2}\|\boldsymbol{B} - \boldsymbol{F}\Theta\Phi\|_{\mathscr{F}}^2\right), \\ p(\boldsymbol{\Theta}|\boldsymbol{\gamma}) &= \prod_{i=1}^{d_\gamma} p(\boldsymbol{\Theta}_{[i]}|\boldsymbol{\gamma}_i) \propto \prod_{i=1}^{d_\gamma} \exp\left(-\tfrac{\gamma_i}{2}\|\boldsymbol{\Theta}_{[i]}\|_{\mathscr{F}}^2\right), \\ p(\boldsymbol{\Phi}|\boldsymbol{\alpha}) &= \prod_{t=1}^{T} \mathcal{N}(\boldsymbol{\varphi}_t|\boldsymbol{0}, \mathrm{diag}(\boldsymbol{\alpha}^{-1})) \propto \prod_{t=1}^{T} \exp\left(-\tfrac{1}{2}\boldsymbol{\varphi}_t^\top \mathrm{diag}(\boldsymbol{\alpha})\boldsymbol{\varphi}_t\right). \end{aligned} \tag{7}$$

To solve the Bayesian inference problem, SI-STBF employed the variational Bayesian (VB) technique to obtain approximated posteriors $q(\boldsymbol{\Theta}, \boldsymbol{\Phi}) \approx p(\boldsymbol{\Theta}, \boldsymbol{\Phi}|\boldsymbol{B})$ by maximizing the *free energy* [42,32,27]

$$\mathscr{F} = \left\langle \log p(\boldsymbol{B}, \boldsymbol{\Theta}, \boldsymbol{\Phi}) - \log q(\boldsymbol{\Theta}, \boldsymbol{\Phi}) \right\rangle_{q(\boldsymbol{\Theta}, \boldsymbol{\Phi})}, \tag{8}$$

where $\langle \cdot \rangle_{q(x)}$ denotes expectation with respect to $q(x)$. To further enable computational tractability, SI-STBF assumed that $q(\boldsymbol{\Theta}, \boldsymbol{\Phi})$ factorizes over groups of parameters:

$$q(\boldsymbol{\Theta}, \boldsymbol{\Phi}) = q(\boldsymbol{\Phi}) \prod_{k=1}^{K} q(\boldsymbol{\theta}_k). \tag{9}$$

The variational posteriors $q(\boldsymbol{\Phi})$ and $q(\boldsymbol{\theta}_k)$, and the hyperparameters $\boldsymbol{\alpha}$ and $\boldsymbol{\gamma}$ were iteratively updated by maximizing the *free energy* (see a detailed description in [27]). The detailed derivation and update rules are presented in the supplementary document. Fig. 1 presents the schematic of SI-STBF. Finally, we can compute the point estimates of the source activities as $\boldsymbol{S} = \boldsymbol{A}\bar{\boldsymbol{\Theta}}\bar{\boldsymbol{\Phi}}$, where $\bar{\boldsymbol{\Theta}}$ and $\bar{\boldsymbol{\Phi}}$ are the variational posterior means of $\boldsymbol{\Theta}$ and $\boldsymbol{\Phi}$, respectively.

2.2. Constructing covariance components from fMRI and EEG data

The CCs $\{\boldsymbol{C}_i\}$ encode the prior spatial information of brain activities, which can be constructed in a data-independent or a data-dependent manner. For the data-independent approach, one example is to set $\boldsymbol{C}_1 = \boldsymbol{I}$, which leads to MNE-like estimations. If $\boldsymbol{C} = \{\boldsymbol{e}_i\boldsymbol{e}_i^\top, i = 1, \ldots, N_s\}$, where $\boldsymbol{e}_i$ is an indexing vector of zeros with a '1' for the i^{th} dipole, then we obtain SBL-like solutions [16].

For the data-dependent method, one can construct CCs from EEG or fMRI data. In our previous work [27], the SI-STBF algorithm derived the CCs from EEG data using the data-driven parcellization (DDP) method and local smoothness constraint [24]. DDP is based on the prelocalization of sources using the multivariate source pre-

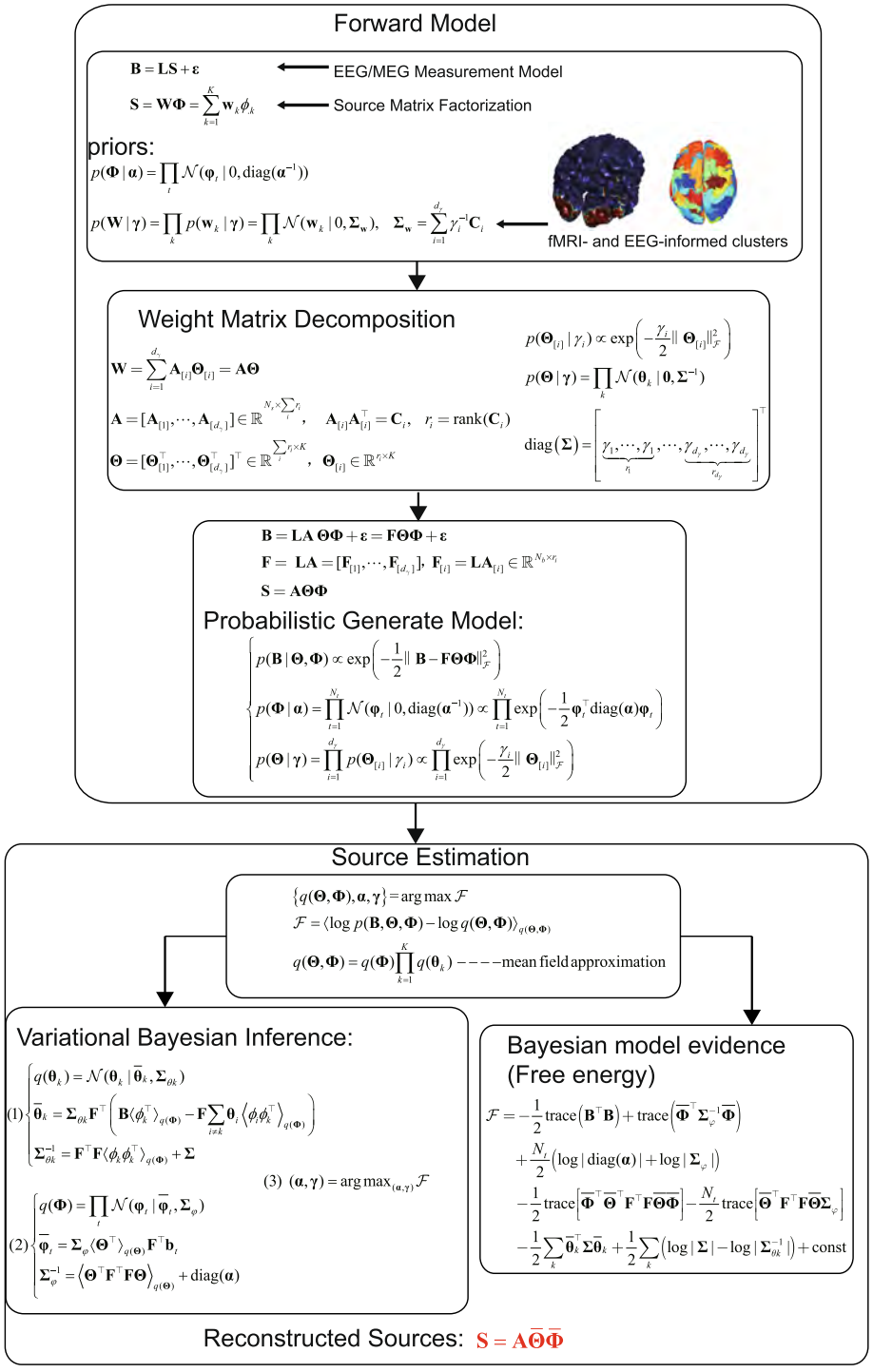

Fig. 1. Schematic of the fMRI-SI-STBF inversion scheme.

localization (MSP), and a region growing algorithm. MSP estimates a coefficient, characterizing the possible contribution of each dipole to the EEG data [43]. After MSP, seed points are selected among the dipoles with the highest MSP coefficients. Then, the region growing around each seed is iterated until a specified spatial neighborhood order s ($s = 4$ in this work), leading to M locally coherent clusters covering the whole cortical surface, and each dipole is assigned to a specified cluster. Then, the Green function $\mathbf{Q}_G$ based on the graph Laplacian matrix $\boldsymbol{G}$ was used to construct the CCs. Specifically, the discrete Laplacian matrix $\boldsymbol{G} \in \mathbb{R}^{N_s \times N_s}$ was first computed based on the adjacency matrix $\mathscr{A} \in \mathbb{R}^{N_s \times N_s}$ ($\mathscr{A}_{ij} = 1$ if j is the adjacent node with link to i, and $\mathscr{A}_{ij} = 0$ otherwise).

$$\boldsymbol{G}_{ij} = \begin{cases} -\sum_{k=1}^{N_s} \mathscr{A}_{ik}, & i = j \\ \mathscr{A}_{ij}, & i \neq j \end{cases} \tag{10}$$

To smooth the Laplacian matrix, the Green function of the Laplacian matrix is then approximated with the Taylor form as $\boldsymbol{Q}_G = \exp(\sigma \boldsymbol{G}) \approx \sum_{\kappa=0}^{8} \frac{\sigma^\kappa}{\kappa!} \boldsymbol{G}^\kappa$, where σ is a positive scalar that controls the spatial smoothness. As suggested in [44], we set $\sigma = 0.6$.

Finally, based on the Green function and the M clusters of DDP, SI-STBF obtains $\mathscr{K}_{\text{EEG}}$ EEG-informed CCs: $\{\boldsymbol{C}_1, \boldsymbol{C}_2, \ldots, \boldsymbol{C}_{\mathscr{K}_{\text{EEG}}}\}$, where $\boldsymbol{C}_i \in \mathbb{R}^{N_s \times N_s}$ is a block matrix generated from the elements of $\boldsymbol{Q}_G^\top \boldsymbol{Q}_G$, with the block being extracted from the row and column indices of the i^{th} cluster, and is zero elsewhere [24].

To incorporate the spatial information of fMRI, in this work, we also constructed CCs from fMRI activation beyond the EEG-informed CCs. The process to construct fMRI-informed CCs consists of five steps: (1) fMRI preprocessing, including realignment, slice timing correction, normalization, and spatial smoothing; (2) statistical analysis of the preprocessed fMRI data using the general linear model (GLM) to obtain the statistical parameter map (SPM); (3) thresholding the SPM to obtain local contiguous voxel clusters; (4) projecting these distinct voxel clusters onto the cortex to obtain $\mathscr{K}_{\text{fMRI}}$ cortical clusters; and (5) constructing $\mathscr{K}_{\text{fMRI}}$ fMRI-informed CCs: $\{\boldsymbol{C}_1, \boldsymbol{C}_2, \ldots, \boldsymbol{C}_{\mathscr{K}_{\text{fMRI}}}\}$, where $\boldsymbol{C}_j \in \mathbb{R}^{N_s \times N_s}$ is a block matrix derived using the elements of $\boldsymbol{Q}_G^\top \boldsymbol{Q}_G$, with the block being extracted from the row and column indices of the j^{th} fMRI clusters. In this work, steps (1) to (4) were conducted in SPM 12 [45].

The EEG-informed and fMRI-informed CCs encode different spatial prior activities of EEG and fMRI data. To construct these CCs, cortical clusters are necessary. An example of fMRI-informed and EEG-informed clusters is shown in Fig. 2. The DDP analysis [24] parcels the whole tessellated cortex into several clusters based on the EEG recordings (as shown in Fig. 2(b)). On the other hand, the fMRI-informed clusters indicate the spatial activities of the fMRI signal (Fig. 2(a)). We assume that the sources in each cluster have functional homogeneity activities. Based on the EEG-informed and fMRI-informed clusters, we obtained EEG-informed and fMRI-informed spatial CCs using the Green function. The contribution of each spatial prior is then automatically determined by the EEG signals under the empirical Bayesian framework. Therefore, we can fuse the spatial information from EEG and fMRI signals to improve the performance of brain source estimation.

Remark 1. During the numerical and experimental data analyses, we used a laptop (i7-8550U CPU 1.8 GHz and 16 GB RAM) for numerical experiments. To derive the EEG-informed CCs, the clustering scale of DDP was set to 4. For $N_b = 70, N_s = 8196$, the number of EEG-informed CCs is approximately 230. With five fMRI-informed CCs, if we set the number of initial TBFs $K = 10$, fMRI-SI-STBF converges after about 200 iterations, which takes less than 3 min. The computational time can be further reduced by skipping the free energy evaluation. To facilitate reproducibility, we uploaded the source code of the proposed method to GitHub, which is available at https://github.com/deep-bci/fMRI-SI-STBF.

3. Method evaluation and performance metrics

3.1. Benchmark source imaging algorithms

The following alternative source imaging algorithms were employed as benchmark methods in this work to assess their accuracy in recovering underlying source activities. (1) wMNE [46], which assumes the source prior to be $p(\boldsymbol{S}) = \prod_{t=1}^{N_t} p(\boldsymbol{s}_t) = \prod_{t=1}^{N_t} \mathcal{N}(\boldsymbol{s}_t | 0, \lambda \boldsymbol{W})$, where $\boldsymbol{W}$ is a $N_s \times N_s$ diagonal matrix and $W_{ii} = \frac{1}{\|\boldsymbol{L}_i\|_2^2}$; (2) fwMNE [35,47,37], which assumes the prior covariance $\lambda \boldsymbol{W}$ is a diagonal matrix as wMNE, and sets the diagonal terms of $\boldsymbol{W}$ corresponding to the locations in fMRI activations to be 1.0, and the other diagonal elements to be 0.1; (3) LORETA [13]; (4) SI-STBF [27], which only uses EEG-informed CCs; (5) SI-SBF [16,27], which employs the same spatial prior as SI-STBF and assumes that the prior of brain sources is $p(\boldsymbol{S}) = \prod_{t=1}^{N_t} p(\boldsymbol{s}_t) = \prod_{t=1}^{N_t} \mathcal{N}\left(\boldsymbol{s}_t | \boldsymbol{0}, \sum_{i=1}^{d_\gamma} \gamma_i^{-1} \boldsymbol{C}_i\right)$; (6) fMRI-SI-SBF, which employs both the EEG-informed and fMRI-informed CCs in SI-SBF; (7) SBL [16]. The regularization parameters of wMNE, fwMNE and LORETA were learned using the Bayesian minimum-norm method [14,27,2]. SI-SBF is an extension of SBL, and its update rules can be found in [16]. FMRI-SI-SBF shares similar prior to the study in [9], and is regarded as the approximation of the method in [9] during this work. Among the compared methods, wMNE, LORETA, SI-STBF, and SI-SBF merely consider EEG data, while fMRI-SI-STBF, fMRI-SI-SBF, and fwMNE make use of both EEG and fMRI data.

3.2. Simulated data

For the simulated data, the lead-field matrix was generated using SPM 12 with a normal resolution (8196 sources) boundary element model (BEM) model, based on the 70-channel EEG sensor configuration of the real EEG data from "multisubject, multimodal face processing" (https://openneuro.org/datasets/ds000117/) [45]. Here, we used EEG and fMRI from Sub01 for the numerical simulation. Following the SPM script along with the dataset to analyze fMRI data of Sub01, an SPM of the T-statistic was created, which compared faces (familiar + unfamiliar) against the baseline. The SPM{T} image was thresholded for $p < 0.05$ (family-wise error corrected across the whole brain). Since the typical brain activated

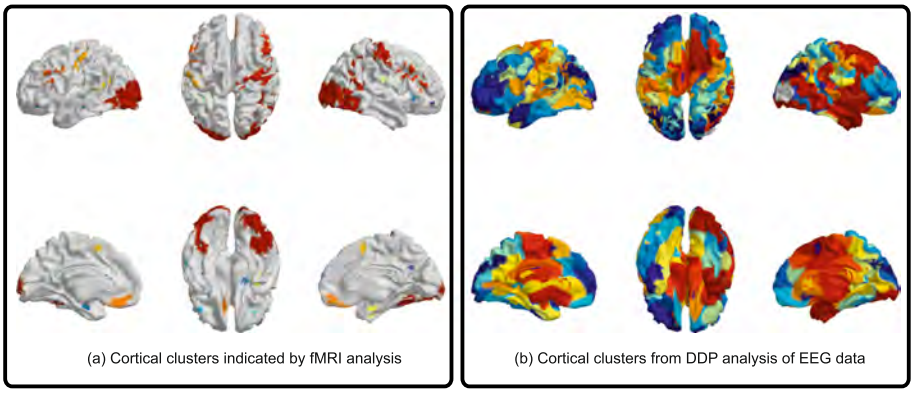

Fig. 2. An example of fMRI-informed and EEG-informed clusters (different colors represent different clusters). (a) Cortical clusters indicated by fMRI analysis of faces (familiar + unfamiliar) vs. baseline from Sub 01 of the "multisubject, multimodal face processing" dataset. (b) EEG-informed clusters using DDP analysis of EEG data.

area associated with detectable changes in EEG is larger than 6 cm^2 [18], small clusters less than a certain number of voxels (10 in this work) were removed. Projecting the voxel fMRI activated clusters onto the cortex, we obtained 22 clusters on the cortical mesh, as shown in Fig. 2(a). Based on the fMRI clusters, we obtained 22 fMRI-informed CCs, as described in Section 2.2. To test the influence of "invalid" fMRI priors, we further created "invalid" fMRI voxel clusters by reflecting the original SPM{T} image in the *y*- and *z*-directions [9]. Projecting the "invalid" fMRI SPM{T} image to the cortex, we obtained 17 invalid-fMRI-informed CCs, which were employed to introduce confounds during the numerical simulations.

To generate the simulated EEG signals, we randomly selected 3 clusters from the 22 valid fMRI indicated patches as active sources. For the time courses, we applied the SVD on the average face EEG data of Sub 01. The time window was 1000 ms (500 time samples with a sampling rate of 500 Hz), starting 200 ms before stimulus onset. We deployed the first three singular vectors over the three

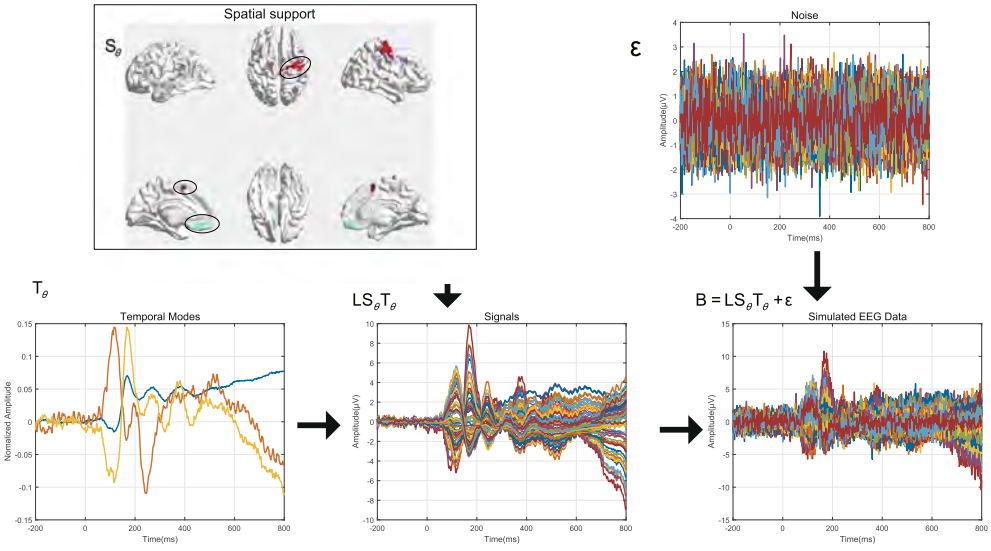

Fig. 3. The procedure to generate synthetic data.

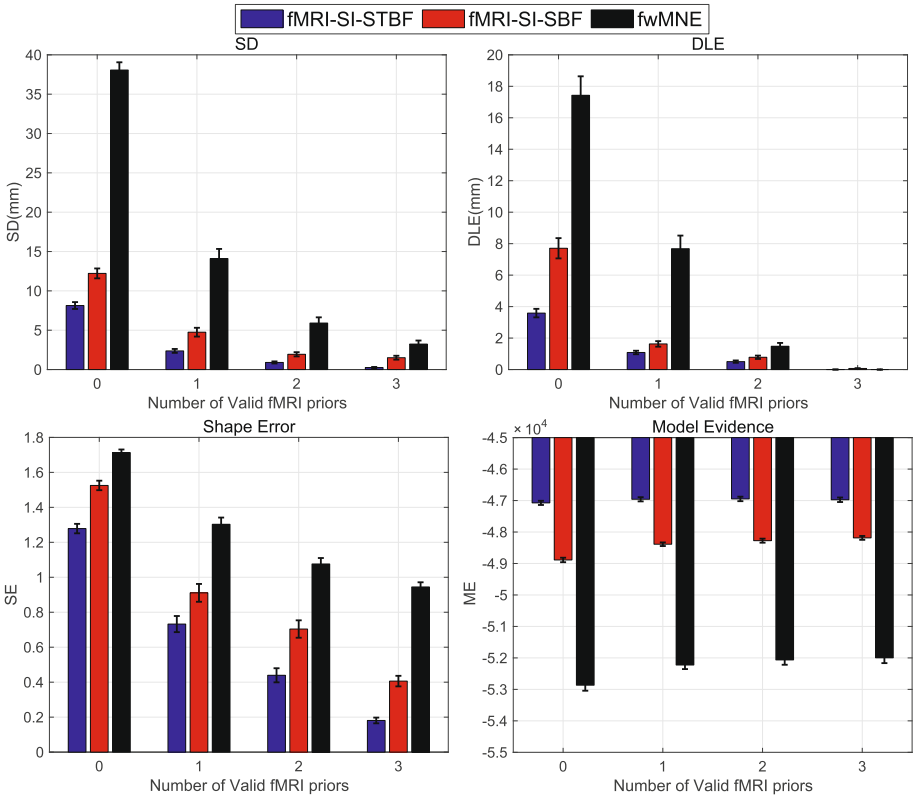

Fig. 4. Performance metrics with varying numbers of valid fMRI priors (SNR = 5 dB).

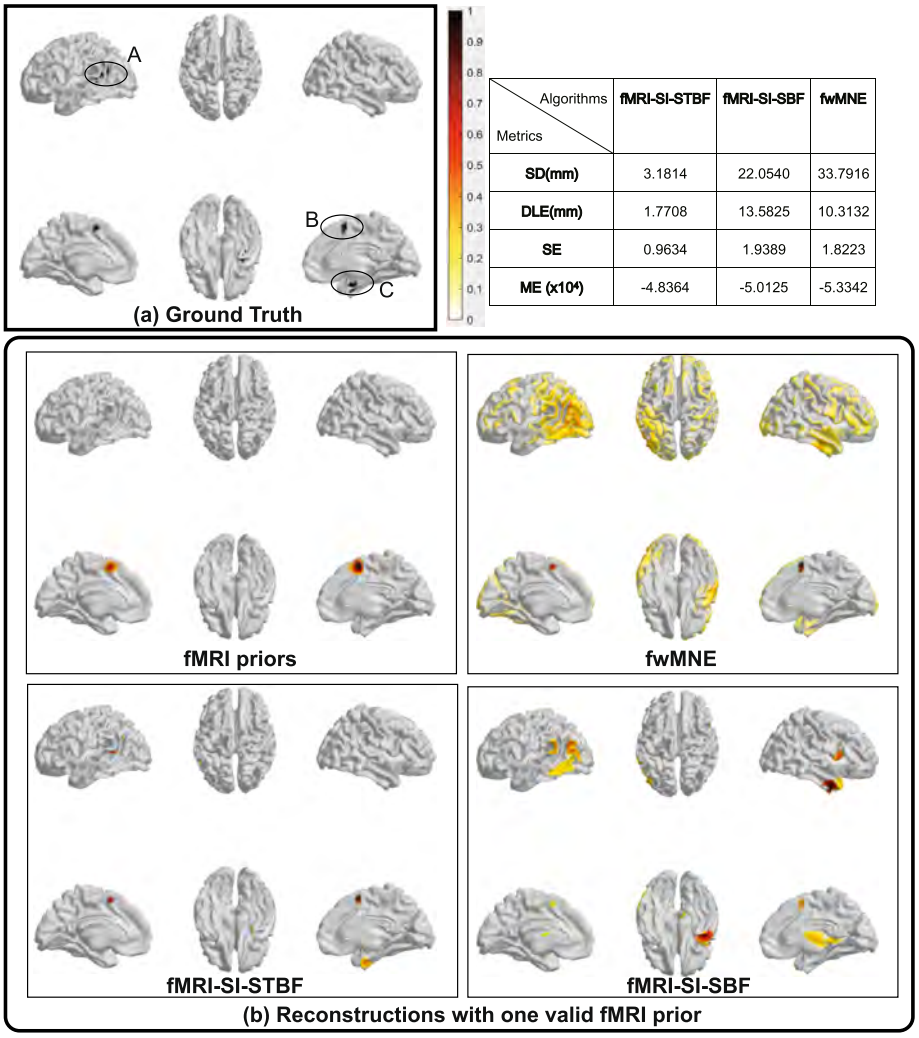

Algorithms / Metrics	fMRI-SI-STBF	fMRI-SI-SBF	fwMNE
SD(mm)	3.1814	22.0540	33.7916
DLE(mm)	1.7708	13.5825	10.3132
SE	0.9634	1.9389	1.8223
ME (x10⁴)	-4.8364	-5.0125	-5.3342

Fig. 5. An imaging example with one valid fMRI prior (SNR = 5 dB). (a) The simulated sources; (b) Reconstruction with one valid fMRI prior (activity of Source B is reflected in fMRI).

selected cortical clusters. The time courses of the dipoles within each cluster were assumed to be the same. Then, the simulated source activities were projected to the EEG sensor space through the lead-field matrix. Finally, white Gaussian measured noise was added to achieve the desired signal-to-noise ratio (SNR), which is defined as: $\mathrm{SNR} = 20\log_{10}\frac{\|\boldsymbol{LS}\|_{\mathscr{F}}}{\|\boldsymbol{\varepsilon}\|_{\mathscr{F}}}$. Fig. 3 depicts the procedure to generate synthetic data.

For the numerical simulations, the following scenarios were considered to evaluate the algorithmic performance of different methods:

1. Varying number of valid fMRI priors. To test the effect of valid fMRI priors, we compared fMRI-SI-STBF, fMRI-SI-SBF and fwMNE using various numbers of valid fMRI-informed CCs. Within this scenario, the number of accurate fMRI priors (CCs that were consistent with the ground truth) varied from 0 to 3.
2. Varying number of invalid fMRI priors. To assess the robustness of fMRI-SI-STBF, fMRI-SI-SBF, and fwMNE, we varied the number of invalid fMRI-informed CCs (i.e., 0, 2, 4, 6, 8), which were randomly selected from the set of CCs derived from the "invalid" fMRI SPM{T} image. For each number of invalid fMRI priors, two accurate fMRI-informed CCs (i.e., CCs consistent with the simulated sources) were also employed.
3. EEG signals with different SNRs. To assess the sensitivity to the SNR, EEG signals with four levels of SNRs (i.e., 10, 5, 0, and −5 dB) were simulated. Furthermore, two valid fMRI-informed and three invalid fMRI-informed CCs were used for source reconstruction.

The SNRs of EEG in scenarios 1 and 2 were set to 5 dB. For each scenario, 100 Monte-Carlo simulations were carried out.

3.3. Performance metrics

The source reconstruction performance was evaluated using the spatial dispersion (SD), distance of localization error (DLE), shape error (SE), and model evidence (ME). Among them, the SD measures the spatial blurredness of the estimated source compared to the ground truth [48,22]; the DLE measures the localization error of the estimated source [48,22]; and the SE quantifies the estimation error in the temporal profiles of the estimated source, which is defined as the squared error between the normalized estimated and simulated sources [49]. Details of how to calculate SD, DLE, and SE are provided in [34]. The ME is a measure that accounts for both data fit and model complexity, and is defined as the log of the marginal likelihood, which is approximated by $\mathscr{F}$ in (8) for SI-

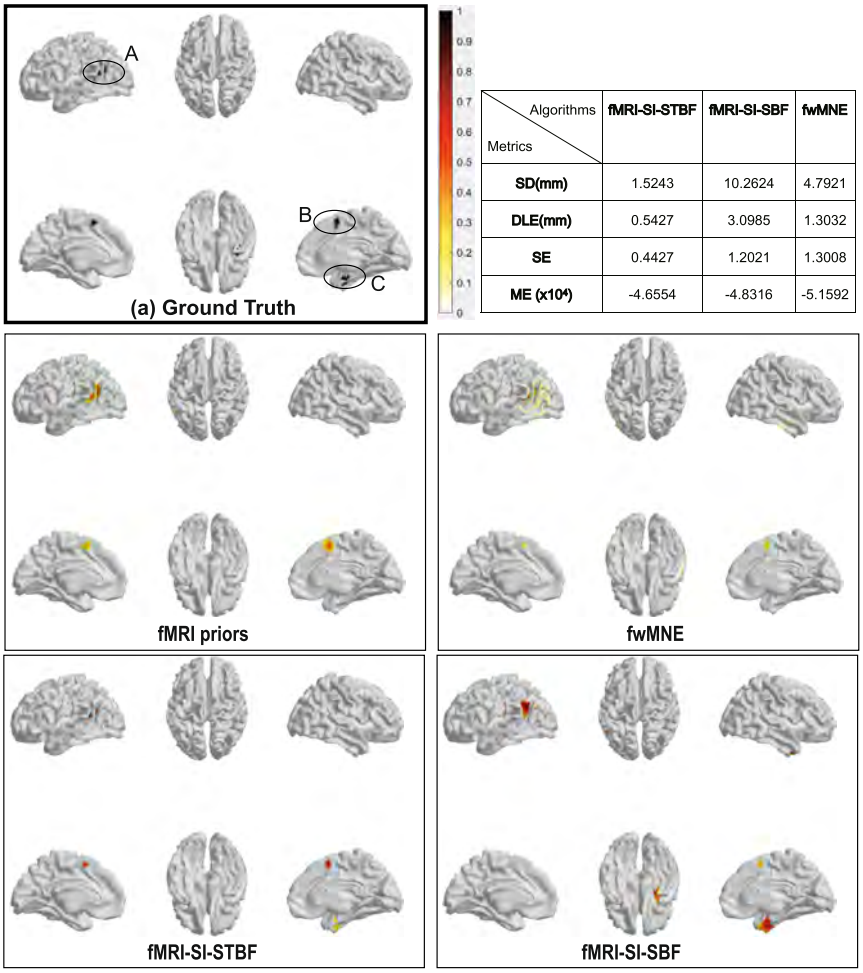

Metrics \ Algorithms	fMRI-SI-STBF	fMRI-SI-SBF	fwMNE
SD(mm)	1.5243	10.2624	4.7921
DLE(mm)	0.5427	3.0985	1.3032
SE	0.4427	1.2021	1.3008
ME (x10⁴)	-4.6554	-4.8316	-5.1592

Fig. 6. An imaging example with two valid fMRI priors (SNR = 5 dB). (a) The simulated sources, which are identical to Fig. 5(a); (b) Reconstruction with one valid fMRI prior (activities of Sources A and B are reflected in fMRI).

STBF and fMRI-SI-STBF. A better source imaging method is expected to yield lower SD, DLE, and SE values, as well as higher ME values.

The Kruskal–Wallis test was employed to test whether the performance of these methods differed significantly. If the difference was significant, then Bonferroni-corrected Wilcoxon rank sum tests were subsequently performed to determine which method significantly outperformed the others. To visualize the results, the imaging maps were thresholded by Otsu's method [34,50].

3.4. Experimental data

To further assess the effectiveness of fMRI-SI-STBF in analyzing real data, we used a 16-subject public dataset from a multimodal neuroimaging study on face perception [39] to compare the model evidence of all the considered methods. This dataset was obtained from the OpenNeuro database, with an accession number of ds000117 (https://openneuro.org/datasets/ds000117/versions/1.0.2). The EEG and fMRI data were acquired separately in this dataset. The experimental paradigm involves a randomized presentation to each subject of approximately 150 familiar faces, 150 unfamiliar faces and 150 scrambled faces. The detailed experimental design is provided in [39]. The EEG data were recorded from 70 electrodes (using the nose reference), sampled at 1.1 kHz and downsampled to 500 Hz for the offline analyses. The MRI data were collected from a Siemens 3T TIM TRIO (Siemens, Erlangen, Germany), and included a $1 \times 1 \times 1$ mm T1-weighted structural MRI (sMRI) as well as a large number of $3 \times 3 \times \sim 4$ mm T2-weighted fMRI EPI volumes acquired during 9 runs of the same task. A total of 210 volumes were acquired in each run (three initial TRs were discarded to allow saturation of T1 effects).

4. Results

4.1. Results of the simulated data analysis

4.1.1. Impact of the number of valid fMRI priors

We first compared the performance of fMRI-SI-STBF, fMRI-SI-SBF and fwMNE by varying the number of valid fMRI-informed CCs. Three active patch sources were simulated, and the number of valid fMRI-informed CCs was set to 0, 1, 2, and 3. Fig. 4 depicts the mean ± SEM (SEM: standard error of the mean) of the performance metrics over 100 Monte Carlo runs. The source localization performance was improved as the number of valid fMRI priors increased. In particular, all three methods showed decreased SD ($p < 0.05$), DLE ($p < 0.05$), and SE ($p < 0.05$) values with an increasing number of valid fMRI priors. Notably, this improvement was the largest for fwMNE, for which ME also increased. When all

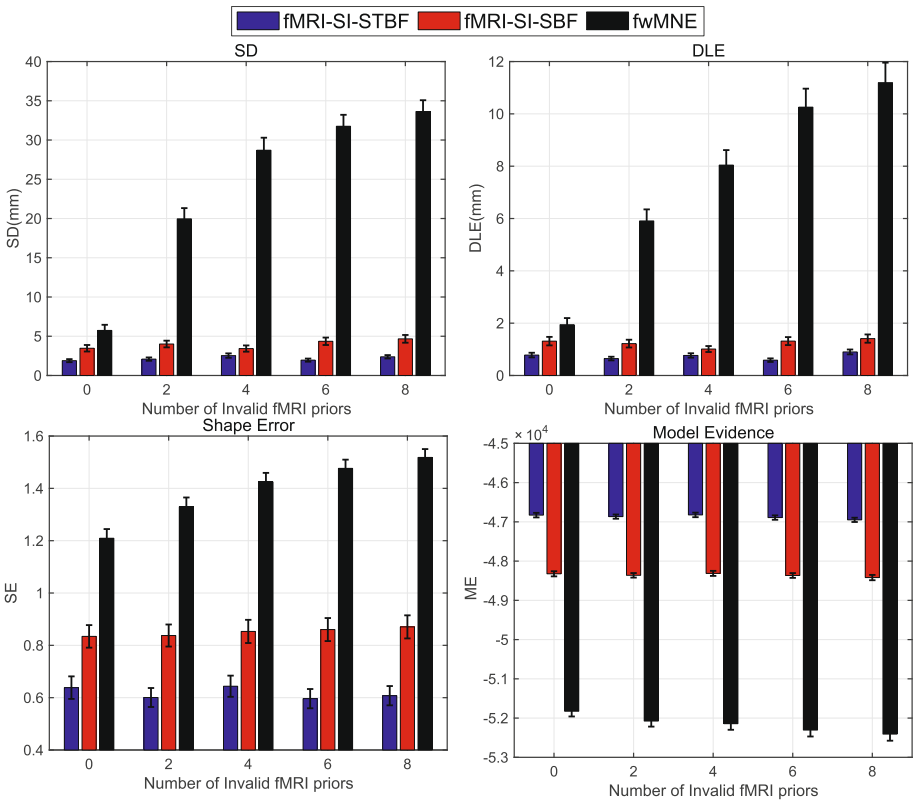

Fig. 7. Performance metrics with various numbers of invalid fMRI priors (SNR = 5 dB).

three valid fMRI CCs were employed, all methods attained nearly zero SD and DLE values. Under all conditions, fMRI-SI-STBF outperformed fMRI-SI-SBF and fwMNE, indicated by the lowest SD ($p < 0.05$), DLE ($p < 0.05$), and SE ($p < 0.05$) values, and the largest ME ($p < 0.05$) values.

Figs. 5 and 6 show an imaging example from a randomly chosen Monte Carlo run. Three simulated clusters were located in the supramarginal area (Source A), superior frontal area (Source B), and right temporal pole (Source C) (Fig. 5(a)). When only one valid fMRI prior (activity of Source B) was available (Fig. 5(b)), fwMNE accurately localized Source B, but the estimate was too diffuse around Sources A and C. Moreover, there were spurious sources at the temporal, frontal, and parietal lobes. fMRI-SI-SBF reconstructed the three clusters well, but produced spurious activities in the middle temporal and thalamus areas. Using both spatial and temporal constraints, fMRI-SI-STBF successfully localized all three simulated clusters. With more valid fMRI priors (Fig. 6), where fMRI indicated the activations of Sources A and B, all three methods can more accurately localize the simulated clusters. However, fwMNE again produced diffused estimates around Source A. Although the activity of Source C was recovered by fwMNE, it did not exceed Otsu's threshold. Moreover, the three ESI methods yielded better performance metrics when more valid fMRI priors were employed. Comparing the results of Figs. 5 and 6, the addition of valid fMRI priors can improve the reconstruction accuracy and help mitigate the diffusion and spuriousness of the source estimation, which is more apparent for fwMNE.

4.1.2. Impact of the number of invalid fMRI priors

In realistic settings, only part of the CCs extracted from fMRI may be related to the EEG signal. To investigate the effect of misspecified priors on fMRI-SI-STBF, we set the number of valid fMRI priors to two, while the number of invalid fMRI priors varied progressively from zero to eight. The results of the statistical analysis over 100 runs are shown in Fig. 7. fwMNE was significantly influenced by the number of invalid fMRI priors, as indicated by increased SD ($p < 0.05$), DLE ($p < 0.05$), and SE ($p < 0.05$) values, and decreased ME ($p < 0.05$) with an increasing number of invalid fMRI priors. Previous studies have confirmed that solutions under the PEB framework are not sensitive to inaccurate priors, when both accurate and inaccurate priors are employed [37]. Since fMRI-SI-STBF and fMRI-SI-SBF are extensions of the PEB framework, they both inherit the intrinsic robustness of PEB, and are not heavily influenced by the number of invalid fMRI priors. This robustness is critical for practical ESI with fMRI priors, where the reliability of priors from fMRI is typically unclear. Moreover, modeling the temporal structure of the EEG signal boosts the performance of fMRI-SI-STBF over fMRI-SI-SBF, as indicated by smaller DLE ($p < 0.05$) and SE ($p < 0.05$) values and larger ME ($p < 0.05$) values.

Fig. 8 depicts an imaging example from a randomly chosen Monte Carlo run with eight invalid fMRI priors. Invalid fMRI priors heavily undermined the performance of fwMNE, as indicated by the diffused and spurious sources around the bilateral fusiform face areas, prefrontal area, and medial orbitofrontal areas. In contrast, fMRI-SI-STBF and fMRI-SI-SBF were not sensitive to invalid fMRI-informed CCs and reconstructed the simulated sources accurately. Indeed, the weights corresponding to invalid fMRI-informed CCs are nearly zero. Fig. 9 shows the corresponding time courses reconstructed by each algorithm. As a result of the temporal smoothness constraint, fMRI-SI-STBF estimated the time courses more accurately than fMRI-SI-SBF and fwMNE, indicated by the larger correlation coefficients between the simulated and reconstructed time courses.

4.1.3. Impact of the SNR

Fig. 10 shows the performance metrics of fMRI-SI-STBF and the benchmark algorithms under varying SNRs. As expected, the per-

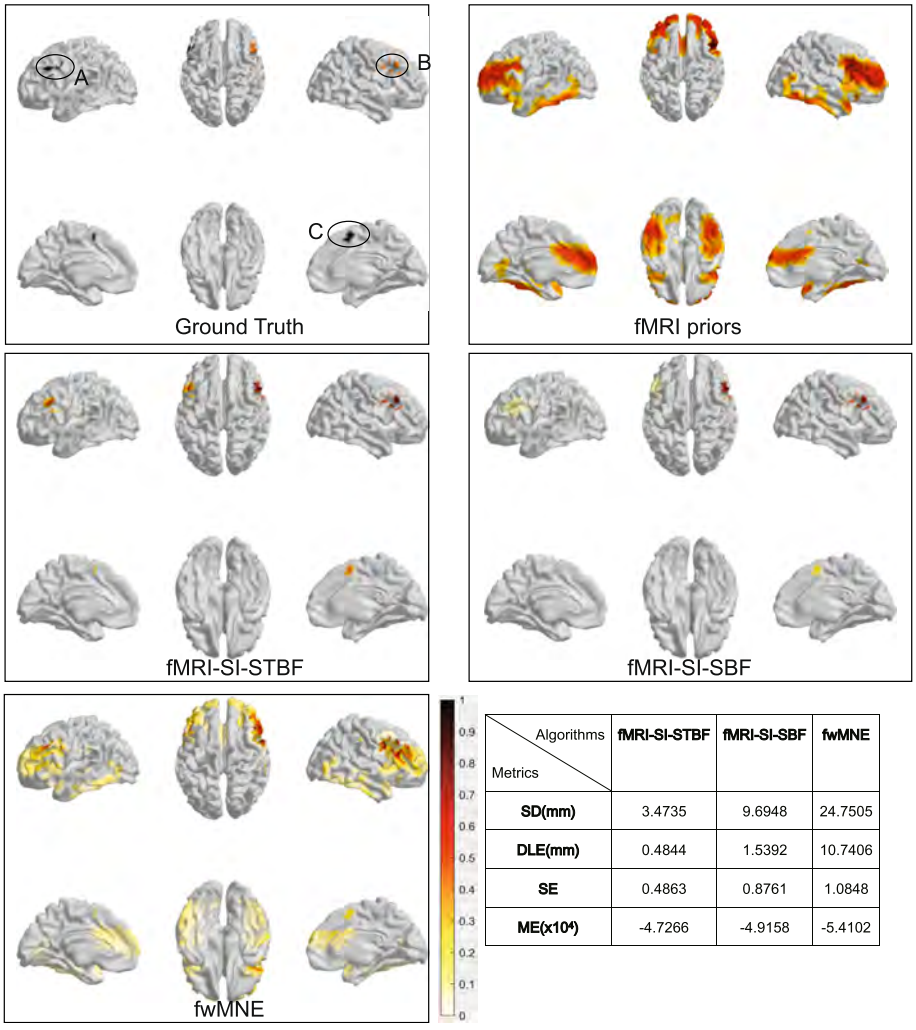

Metrics \ Algorithms	fMRI-SI-STBF	fMRI-SI-SBF	fwMNE
SD(mm)	3.4735	9.6948	24.7505
DLE(mm)	0.4844	1.5392	10.7406
SE	0.4863	0.8761	1.0848
ME(x10⁴)	-4.7266	-4.9158	-5.4102

Fig. 8. An imaging example with eight invalid fMRI priors (SNR = 5 dB).

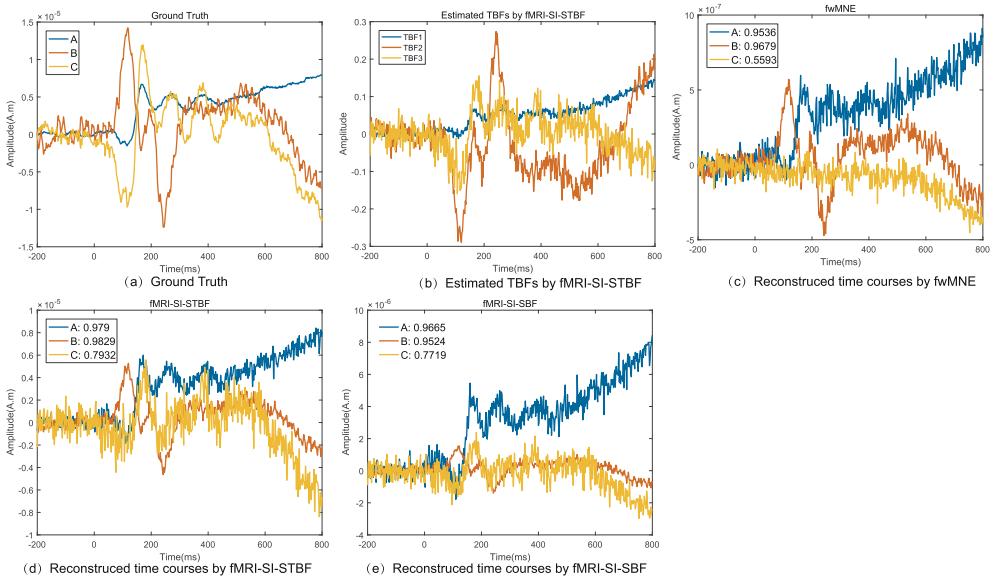

Fig. 9. Reconstructed time courses with eight invalid fMRI priors (SNR = 5 dB). (a) Simulated time courses for the three sources; (b) estimated TBFs by SI-STBF; (c)–(e) reconstructed (mean) time courses by fMRI-SI-STBF, fMRI-SI-SBF and fwMNE. The correlation coefficients of the simulated and estimated time courses are shown at the top-left corner of each subfigure.

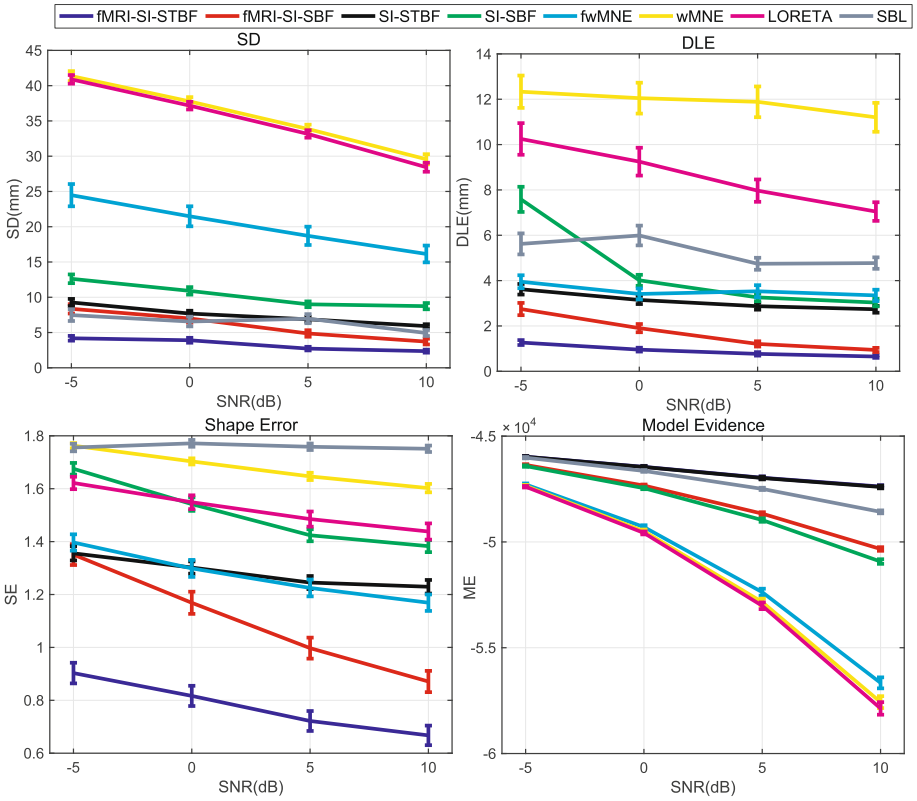

Fig. 10. Performance metrics under various SNR levels. The curves of model evidence from SI-STBF and fMRI-SI-STBF overlapped.

formance of all methods declined as the SNR increased. Moreover, methods incorporating fMRI information outperformed those without fMRI information (i.e., fMRI-SI-STBF vs. SI-STBF, fMRI-SI-SBF vs. SI-SBF, fwMNE vs. wMNE), indicated by smaller SD, DLE and SE values. Interestingly, there was little improvement in the ME with the addition of fMRI priors to SI-STBF, as seen by the nearly overlapping curves of the ME for fMRI-SI-STBF and SI-STBF. This result suggests that the CCs from DDP of EEG may already be optimal for SI-STBF. Due to the Student's-*t* prior induced by automatic relevance determination (ARD), SBL yielded overly sparse solutions and missed most of the other dipoles within the active clusters [14], which led to larger time course profile errors of active sources, indicated by the large SE values. For all SNRs, fMRI-SI-STBF achieved the lowest SD, DLE, and SE values, as well as the largest ME values among the compared methods.

Figs. 11 and 12 present an imaging example from a randomly chosen Monte Carlo run with SNR = 5 dB. Two clusters around the bilateral rostral middle frontal gyrus (Sources A and C) and one cluster with much larger extent in the precentral area (Source B) were simulated. SBL only localized several point sources near the ground truth. wMNE obtained estimates encompassing most of the cortex. LORETA provided smooth and continuous estimates around Source B. In fact, LORETA also obtained estimates around Sources A and C that did not exceed Otsu's threshold. Although fwMNE improved the spatial resolution of wMNE when fMRI priors were employed, it also suffered from spurious sources in the right posterior cingulate area introduced by invalid fMRI priors. Since EEG-informed CCs are highly effective for reconstructing the activations in this example, there is little difference between the results of fMRI-SI-STBF, fMRI-SI-SBF, SI-STBF, and SI-SBF visually. However, fMRI-SI-STBF showed smaller SD, DLE, and SE values as well as larger ME than the benchmark algorithms, as shown in Table 1 of the supplementary document. Combining the results of Figs. 10–12, the fMRI-informed CCs can enhance the performance metrics of SI-STBF and SI-SBF, although the improvement is small visually.

4.2. Results of experimental data analysis

The differential between the averaged ERPs of faces and scrambled faces was used for source imaging. An analysis time window of 1000 ms was considered, ranging from −200 ms to 800 ms relative to the stimulus onset. The lead-field matrix of each subject was computed using SPM12 based on a normal resolution (8,196 sources) BEM model. After fMRI preprocessing, three SPMs of the T-statistic (familiar vs. baseline, unfamiliar vs. baseline, scrambled vs. baseline) were created for each subject. Then group T-statistics were obtained to compare the faces (familiar + unfamiliar) against scrambled faces across subjects. The final SPM{T} was thresholded to identify regions of at least 10 contiguous voxels that survived the threshold for local maxima of $p < 0.05$ (FWE-corrected), which yielded three clusters located at the left and right occipital face area (OFA), and right fusiform face area (FFA) (Fig. 13). EEG/fMRI data preprocessing, SPM analysis of fMRI data, and computation of the lead-field matrix were conducted using SPM12 and MATLAB scripts provided along with the dataset.

Having obtained the three clusters from the group statistic across all 16 subjects, following the study in [45], we used these clusters as fMRI priors for the ESI of each subject. Due to the space limit, we only present the results of Sub 16 in Fig. 14. The results of the remaining 15 subjects are provided in the supplementary document. For each subject, we depict the model evidence and imaging sources of the root-mean-square power within 160–180 ms after stimulus onset. To visualize the estimated sources, imaging results were thresholded using Otsu's method [50].

The reconstructed sources of wMNE and LORETA were dispersed and spread over the bilateral fusiform gyrus and temporal and frontal lobes. With the addition of fMRI priors, fwMNE was

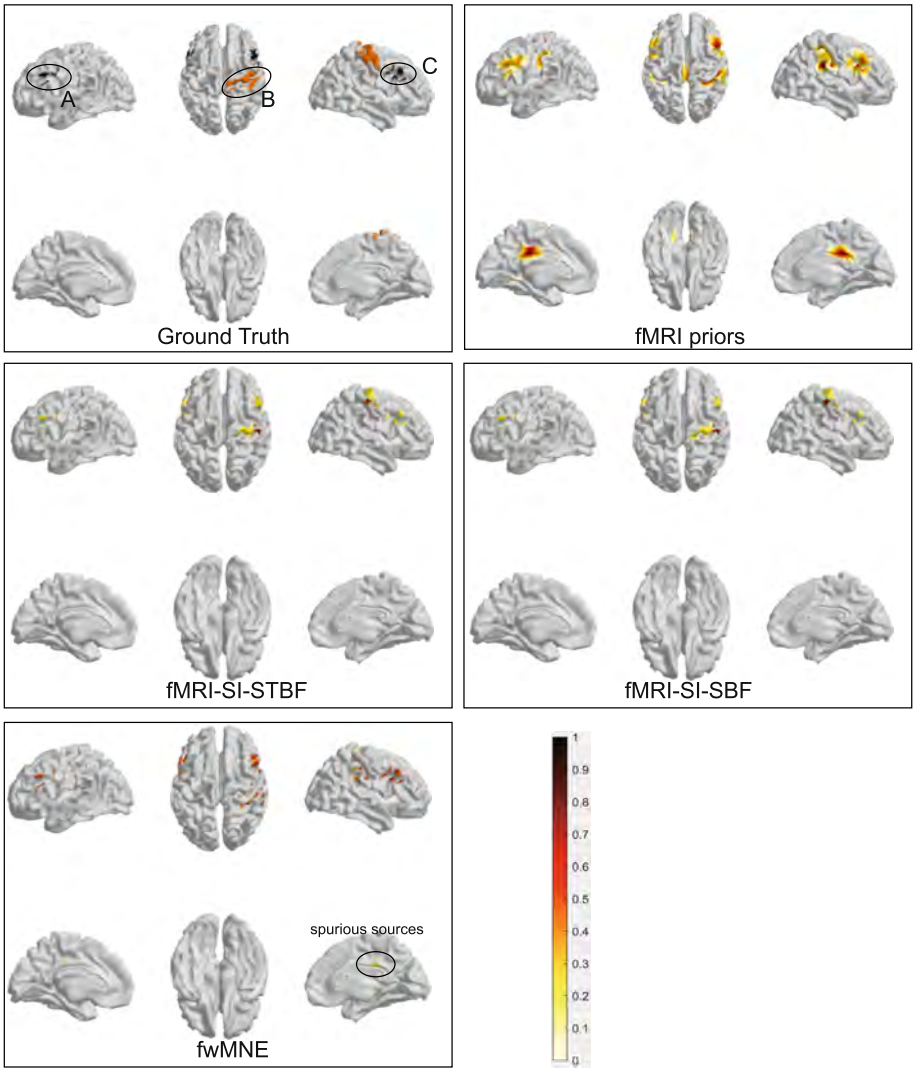

Fig. 11. An imaging example from fMRI-SI-STBF and the benchmark algorithms with fMRI priors under SNR = 5 dB.

able to reveal the right FFA and bilateral OFA, exhibiting a much higher spatial resolution than wMNE. However, fwMNE was too rigidly constrained by the fMRI priors and failed to reveal the activity at the left FFA. On the other hand, SBL identified several point sources distributed in the bilateral FFA and OFA. With locally smooth CCs under the empirical Bayesian framework, SI-STBF and SI-SBF revealed activities in the bilateral FFA and around the inferior temporal gyrus, which were partially in line with the wMNE and LORETA results, but the sources at FFA were more clearly localized. For Sub 06 and 09, SI-SBF either failed to reveal activity at the left FFA or only yielded weak activity that did not exceed Otsu's threshold. Utilizing the spatiotemporal factorization of the source matrix, fMRI-SI-STBF and SI-STBF revealed the left FFA sources better than SI-SBF. With the addition of fMRI-informed CCs, the sources of fMRI-SI-STBF were visually similar to those of SI-STBF.

In terms of the ME, fMRI-SI-STBF and SI-STBF substantially outperformed other source imaging methods, which is also in line with the imaging results. Applying fMRI priors, fwMNE showed markedly larger model evidence than wMNE. For SI-STBF and SI-SBF, the addition of fMRI-informed CCs indicated a general lack of ME improvement, suggesting that EEG-informed CCs may be ready to be optimal for this multimodal face study.

5. Discussion

In this work, we have proposed an fMRI-informed ESI method based on source matrix factorization under the empirical Bayesian framework, fMRI-SI-STBF. Knowledge of fMRI activation from the GLM analysis was encoded with spatial CCs. Using an ARD prior, the proposed method can select the fMRI-informed and EEG-informed CCs that are related to brain activities in an automatic fashion. Additionally, the proposed method incorporated a temporal constraint via current source matrix decomposition, which improved the spatiotemporal resolution of the estimated sources compared to the spatial-only constraints. Monte Carlo simulation and "multimodal face" EEG/fMRI experimental data analysis were performed to validate fMRI-SI-STBF. The simulation results demonstrated that the proposed method could effectively leverage the fMRI information, even when invalid fMRI priors exist.

Many previous studies have employed neuronal-anatomical priors to construct cortical activities. These methods have used spatial priors derived from the spatial information in structural MRI [51], based on the assumption that neighboring dipoles have similar neuronal activities [13,25,14,44] or based on fMRI activation [9,38,35,47]. A method that is widely used for fMRI constrained ESI is fwMNE [35], which employs fMRI activation to

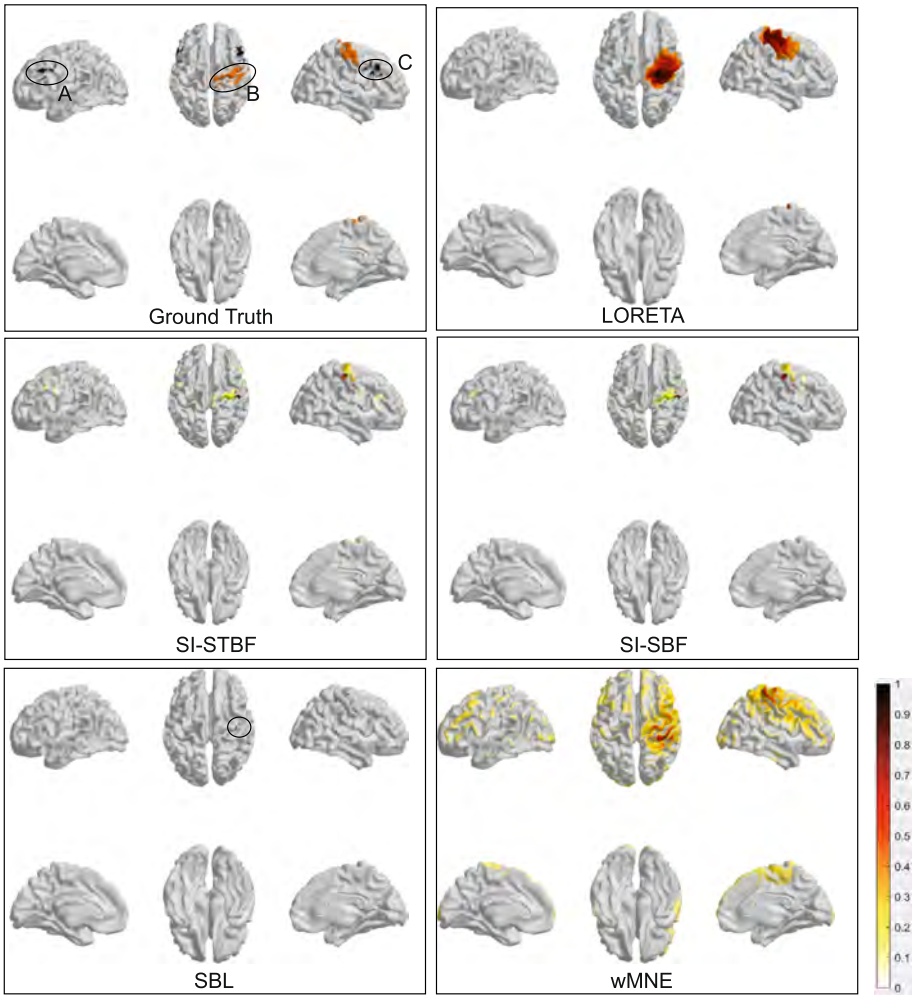

Fig. 12. An imaging example from ESI algorithms without fMRI priors under SNR = 5 dB. The ground truth is identical to Fig. 11(a).

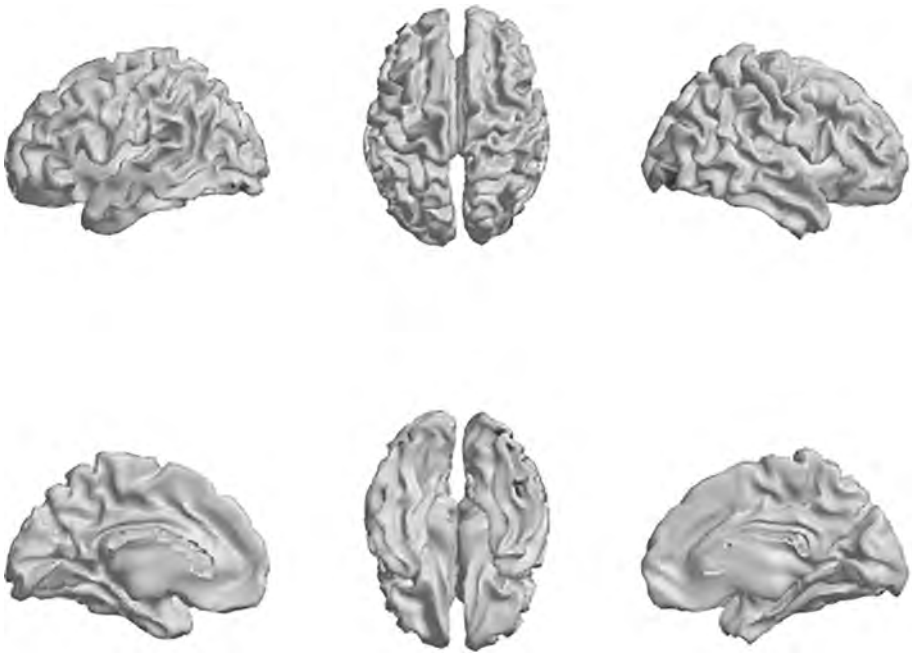

Fig. 13. Group SPM for Faces vs. Scrambled fMRI data thresholded for clusters with at least 10 voxels that survive $p < 0.05$ (FWE-corrected), obtaining three clusters located at right fusiform face area (FFA) and bilateral occipital face area (OFA).

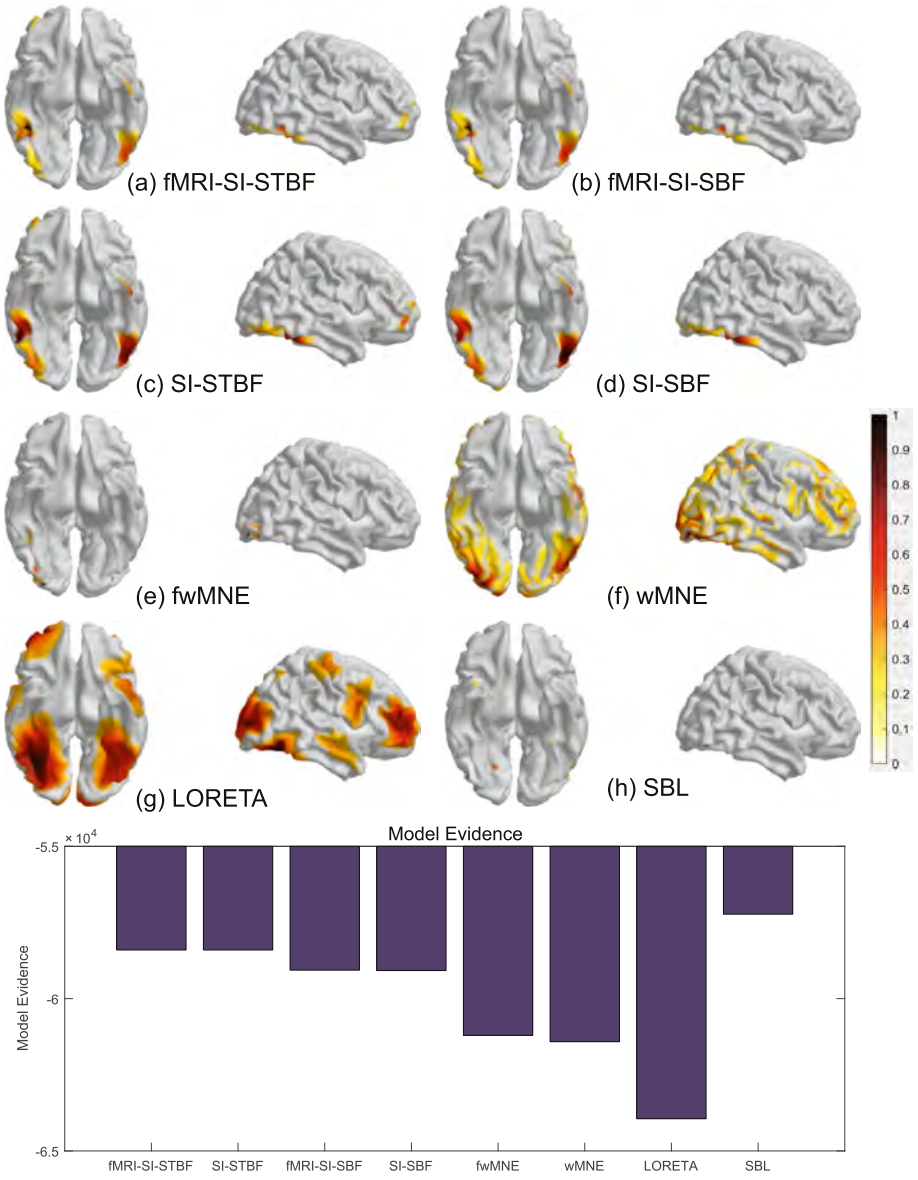

Fig. 14. Estimated sources for face perception of Sub 16. For each algorithm, the ventral view of the cortex is provided on the left, and the lateral view is on the right. The results are presented as the root-mean-square power within 160–180 ms post-stimulus.

construct the weight matrix for wMNE. However, fwMNE is highly sensitive to fMRI priors. When the fMRI priors include invalid or extra activations, spurious sources emerge for fwMNE (see the imaging example in Fig. 8). When some sources are not reflected in fMRI activation, fwMNE tends to miss these sources. For example, the group fMRI analysis for the "multimodal face" study did not reveal the sources at the left FFA (Fig. 13), which are known to be related to face perception [44,9,37]. As a result, the reconstruction for all 16 subjects by fwMNE also failed to reveal activation at the left FFA.

To incorporate fMRI information as a "soft" constraint as opposed to the "hard" constraint in fwMNE, we treated each suprathreshold fMRI cluster as a separate location prior. Each cluster prior was represented by a spatial CC under the empirical Bayesian framework. The relative contribution of each CC is controlled by the corresponding hyperparameters. According to variational Bayesian inference with the ARD prior, fMRI-SI-STBF and SI-STBF automatically select the CCs that can increase the ME. When the fMRI priors are invalid or redundant, they are expected to be automatically pruned in the forward model with the largest ME. As shown in Figs. 7 and 8, fMRI-SI-STBF is not noticeably influenced by invalid fMRI CCs, which is very important for practical data analysis, where the validity of the fMRI priors is often unclear. Moreover, an interesting observation is that fMRI priors only slightly increased ME when using empirical Bayesian and EEG-informed CCs (Figs. 4, 10 and 14). This increase may be attributed to the fact that the fMRI-informed CCs were largely subsumed in the mixture of EEG-informed CCs. Nonetheless, considering the other three performance metrics, as shown in Figs. 4 and 10, employing the valid fMRI priors indeed improved the spatiotemporal accuracy of the estimated sources.

The excellent temporal resolution of EEG signals offers unique temporal structures that can be utilized to improve source reconstruction performance. In fact, the use of temporal information is the main difference between fMRI-SI-STBF and previous PEB-based source imaging methods with fMRI priors [9,37,10]. To reg-

ularize current sources with temporal information, fMRI-SI-STBF represents the source matrix as a linear combination of several TBFs using matrix factorization. With variational Bayesian inference, the TBFs and corresponding weights of each dipole are simultaneously learned from the EEG data. Our numerical results show that the addition of temporal information leads to more accurate spatial estimation and larger correlation coefficients between reconstructed and simulated time courses (see Fig. 9). By fusing the EEG-fMRI spatiotemporal information, fMRI-SI-STBF obtains the lowest reconstruction error of source extents, locations and time courses, indicated by the lowest SD, DLE and SE values, as shown in Figs. 4, 7 and 10. For the experimental data analysis, fMRI-SI-STBF successfully identifies the activities at bilateral FFA areas that are related to face perception, while fMRI-SI-SBF fails to localize the activities at the left FFA for some subjects (e.g., Sub 06, 09, see results in the supplementary document). For all 16 subjects, fMRI-SI-STBF also achieved the largest ME values.

Current work used fMRI priors derived from GLM analysis. However, as previous studies [52,37,10] suggested, the GLM approach requires *a priori* specification of the hemodynamic response function. In contrast, independent component analysis (ICA) as a data-driven approach may be more advantageous than the GLM approach and can still obtain similar loci for task-related activations [52]. In addition, the ICA of fMRI data can yield several temporally coherent networks (TCNs), where the regions within each TCN share the same response pattern. In our future work we will utilize these TCNs instead of the functional activation from GLM analysis in the framework of fMRI-SI-STBF to further improve the source reconstruction performance. Furthermore, with the TCNs identified during a resting-state, fMRI-SI-STBF can be employed to analyze the resting-state EEG/fMRI data. Although in this work we focus on the multimodal face dataset for experimental data analysis, future studies will examine the utility of fMRI-SI-STBF for concurrent EEG/fMRI data analysis to further validate the proposed method. Additionally, deep neural networks (DNNs) have significantly boosted artificial intelligence. Several studies have focused on the architectural design of DNN models [53,54]. We will also employ these techniques to design suitable DNN models for EEG-fMRI source imaging.

6. Conclusion

We proposed an fMRI-informed electromagnetic source imaging method with spatiotemporal constraints based on source matrix decomposition under empirical Bayesian framework. Our simulations using synthetic and experimental data suggest that fMRI-SI-STBF can effectively employ the spatial information from fMRI data and is robust to the "invalid" fMRI priors. The numerical results suggest that fMRI-SI-STBF estimates the extents, locations and time courses of brain activities more accurately than previous ESI algorithms without fMRI constraints (i.e., wMNE, LORETA, SBL, SI-STBF, SI-SBF) and existing ESI methods with fMRI priors (i.e., fwMNE and fMRI-SI-SBF). The proposed method is a promising alternative to reconstruct cortical activities for neuroscience research and clinical diagnosis.

CRediT authorship contribution statement

Ke Liu: Conceptualization, Methodology, Software, Validation, Writing - original draft, Writing - review & editing. **Zhu Liang Yu:** Conceptualization, Supervision, Writing - review & editing. **Wei Wu:** Methodology, Writing - original draft, Writing - review & editing. **Zhenghui Gu:** Validation, Writing - original draft. **Cuntai Guan:** Formal analysis.

Declaration of Competing Interest

The authors declare that they have no known competing financial interests or personal relationships that could have appeared to influence the work reported in this paper.

Acknowledgements

This work was supported in part by the National Natural Science Foundation of China under Grants 61703065, 61836003, 61876063, and 61876201. Chongqing Research Program of Application Foundation and Advanced Technology under Grant cstc2018jcyjAX0151, the Science and Technology Research Program of Chongqing Municipal Education Commission under Grant KJQN201800612.

Appendix A. Supplementary data

Supplementary data associated with this article can be found, in the online version, at https://doi.org/10.1016/j.neucom.2021.06.066.

References

[1] W. Wu, S. Nagarajan, Z. Chen, Bayesian Machine Learning: EEG/MEG signal processing measurements, IEEE Signal Process. Mag. 33 (1) (2016) 14–36.
[2] C. Cai, K. Sekihara, S.S. Nagarajan, Hierarchical multiscale Bayesian algorithm for robust MEG/EEG source reconstruction, NeuroImage 183 (2018) 698–715.
[3] B. He, A. Sohrabpour, E. Brown, Z. Liu, Electrophysiological source imaging: A noninvasive window to brain dynamics, Annu. Rev. Biomed. Eng. 20 (2018) 171–196.
[4] S. Hassantabar, N. Stefano, V. Ghanakota, A. Ferrari, G.N. Nicola, R. Bruno, I.R. Marino, K. Hamidouche, N.K. Jha, Coviddeep: Sars-cov-2/covid-19 test based on wearable medical sensors and efficient neural networks, arXiv preprint arXiv:2007.10497..
[5] S. Dorosti, S.J. Ghoushchi, E. Sobhrakhshankhah, M. Ahmadi, A. Sharifi, Application of gene expression programming and sensitivity analyses in analyzing effective parameters in gastric cancer tumor size and location, Soft Comput. 24 (13) (2020) 9943–9964.
[6] S. Hassantabar, M. Ahmadi, A. Sharifi, Diagnosis and detection of infected tissue of covid-19 patients based on lung x-ray image using convolutional neural network approaches, Chaos Solitons Fract. 140 (2020) 110170.
[7] M. Ahmadi, S. Jafarzadeh-Ghoushchi, R. Taghizadeh, A. Sharifi, Presentation of a new hybrid approach for forecasting economic growth using artificial intelligence approaches, Neural Comput. Appl. 31 (12) (2019) 8661–8680.
[8] X. Chen, X. Xu, A. Liu, S. Lee, X. Chen, X. Zhang, M.J. McKeown, Z.J. Wang, Removal of muscle artifacts from the EEG: a review and recommendations, IEEE Sensors J. 19 (14) (2019) 5353–5368.
[9] R.N. Henson, G. Flandin, K.J. Friston, J. Mattout, A parametric empirical bayesian framework for fMRI-constrained MEG/EEG source reconstruction, Hum. Brain Mapp. 31 (10) (2010) 1512–1531.
[10] X. Lei, T. Wu, P. Valdes-Sosa, Incorporating priors for EEG source imaging and connectivity analysis, Front. Neurosci. 9 (2015) 284.
[11] M.S. Hämäläinen, R. Ilmoniemi, Interpreting magnetic fields of the brain: minimum norm estimates, Med. Biol. Eng. Comput. 32 (1) (1994) 35–42.
[12] R.D. Pascual-Marqui, Standardized low-resolution brain electromagnetic tomography (sLORETA): technical details, Methods Find Exp. Clin. Pharmacol. 24 Suppl D (2002) 5–12..
[13] R.D. Pascual-Marqui, C.M. Michel, D. Lehmann, Low resolution electromagnetic tomography: a new method for localizing electrical activity in the brain, Int. J. Psychophysiol. 18 (1) (1994) 49–65.
[14] K. Liu, Z.L. Yu, W. Wu, Z. Gu, Y. Li, S. Nagarajan, Bayesian electromagnetic spatio-temporal imaging of extended sources with markov random field and temporal basis expansion, NeuroImage 139 (2016) 385–404.
[15] L. Ding, B. He, Sparse source imaging in electroencephalography with accurate field modeling, Hum. Brain Mapp. 29 (9) (2008) 1053–1067.
[16] D. Wipf, S. Nagarajan, A unified Bayesian framework for MEG/EEG source imaging, NeuroImage 44 (3) (2009) 947–966.
[17] D.P. Wipf, J.P. Owen, H.T. Attias, K. Sekihara, S.S. Nagarajan, Robust bayesian estimation of the location, orientation, and time course of multiple correlated neural sources using MEG, NeuroImage 49 (1) (2010) 641–655.
[18] J.X. Tao, A. Ray, S. Hawes-Ebersole, J.S. Ebersole, Intracranial EEG substrates of scalp EEG interictal spikes, Epilepsia 46 (5) (2005) 669–676.
[19] M. Hämäläinen, R. Hari, R.J. Ilmoniemi, J. Knuutila, O.V. Lounasmaa, Magnetoencephalography-theory, instrumentation, and applications to noninvasive studies of the working human brain, Rev. Mod. Phys. 65 (2) (1993) 413–497.

[20] G. Huiskamp, Z. Agirre-Arrizubieta, F. Leijten, Regional differences in the sensitivity of MEG for interictal spikes in epilepsy, Brain Topogr. 23 (2) (2010) 159–164.
[21] A. Sohrabpour, Y. Lu, G. Worrell, B. He, Imaging brain source extent from EEG/MEG by means of an iteratively reweighted edge sparsity minimization (IRES) strategy, NeuroImage 142 (2016) 27–42.
[22] M. Zhu, W. Zhang, D.L. Dickens, L. Ding, Reconstructing spatially extended brain sources via enforcing multiple transform sparseness, NeuroImage 86 (2014) 280–293.
[23] S. Haufe, R. Tomioka, T. Dickhaus, C. Sannelli, B. Blankertz, G. Nolte, K.-R. Müller, Large-scale EEG/MEG source localization with spatial flexibility, NeuroImage 54 (2) (2011) 851–859.
[24] R.A. Chowdhury, Y. Zerouali, T. Hedrich, M. Heers, E. Kobayashi, J.-M. Lina, C. Grova, MEG-EEG information fusion and electromagnetic source imaging: From theory to clinical application in epilepsy, Brain Topogr. 28 (6) (2015) 785–812.
[25] C. Lamus, M.S. Hämäläinen, S. Temereanca, E.N. Brown, P.L. Purdon, A spatiotemporal dynamic distributed solution to the MEG inverse problem, NeuroImage 63 (2) (2012) 894–909.
[26] A. Gramfort, D. Strohmeier, J. Haueisen, M.S. Hämäläinen, M. Kowalski, Time-frequency mixed-norm estimates: sparse M/EEG imaging with non-stationary source activations, NeuroImage 70 (2013) 410–422.
[27] K. Liu, Z.L. Yu, W. Wu, Z. Gu, J. Zhang, L. Cen, S. Nagarajan, Y. Li, Bayesian electromagnetic spatio-temporal imaging of extended sources based on matrix factorization, IEEE Trans. Biomed. Eng. 66 (9) (2019) 2457–2469.
[28] P. Das, C. Brodbeck, J.Z. Simon, B. Babadi, Neuro-current response functions: A unified approach to meg source analysis under the continuous stimuli paradigm, NeuroImage 211 (2020) 116528.
[29] K. Liu, Z.L. Yu, W. Wu, Z. Gu, Y. Li, STRAPS: A fully data-driven spatio-temporally regularized algorithm for M/EEG patch source imaging, Int. J. Neural Syst. 1550016 (2015).
[30] M. Fukushima, O. Yamashita, A. Kanemura, S. Ishii, M. Kawato, M.-A. Sato, A state-space modeling approach for localization of focal current sources from meg, IEEE Trans. Biomed. Eng. 59 (6) (2012) 1561–1571.
[31] M. Fukushima, O. Yamashita, T.R. Knösche, M.-A. Sato, Meg source reconstruction based on identification of directed source interactions on whole-brain anatomical networks, NeuroImage 105 (2015) 408–427.
[32] N.J. Trujillo-Barreto, E. Aubert-Vázquez, W.D. Penny, Bayesian M/EEG source reconstruction with spatio-temporal priors, NeuroImage 39 (1) (2008) 318–335.
[33] A. Bolstad, B.V. Veen, R. Nowak, Space–time event sparse penalization for magneto-/electroencephalography, NeuroImage 46 (4) (2009) 1066–1081.
[34] K. Liu, Z.L. Yu, W. Wu, Z. Gu, Y. Li, S. Nagarajan, Variation sparse source imaging based on conditional mean for electromagnetic extended sources, Neurocomputing 313 (2018) 96–110.
[35] A.K. Liu, J.W. Belliveau, A.M. Dale, Spatiotemporal imaging of human brain activity using functional MRI constrained magnetoencephalography data: Monte carlo simulations, Proc. Nat. Acad. Sci. 95 (15) (1998) 8945–8950.
[36] M.-A. Sato, T. Yoshioka, S. Kajihara, K. Toyama, N. Goda, K. Doya, M. Kawato, Hierarchical Bayesian estimation for MEG inverse problem, NeuroImage 23 (3) (2004) 806–826.
[37] X. Lei, P. Xu, C. Luo, J. Zhao, D. Zhou, D. Yao, fMRI functional networks for EEG source imaging, Hum. Brain Mapp. 32 (7) (2011) 1141–1160.
[38] X. Lei, J. Hu, D. Yao, Incorporating fmri functional networks in EEG source imaging: a Bayesian model comparison approach, Brain Topogr. 25 (1) (2012) 27–38.
[39] D.G. Wakeman, R.N. Henson, A multi-subject, multi-modal human neuroimaging dataset, Sci. Data 2 (2015) 150001.
[40] B. He, L. Yang, C. Wilke, H. Yuan, Electrophysiological imaging of brain activity and connectivity-challenges and opportunities, IEEE Trans. Biomed. Eng. 58 (7) (2011) 1918–1931.
[41] R. Grave de Peralta Menendez, M.M. Murray, C.M. Michel, R. Martuzzi, S.L. Gonzalez Andino, Electrical neuroimaging based on biophysical constraints, NeuroImage 21 (2) (2004) 527–539..
[42] K.P. Murphy, Machine Learning: A Probabilistic Perspective, MIT Press, 2012.
[43] R.A. Chowdhury, J.M. Lina, E. Kobayashi, C. Grova, MEG source localization of spatially extended generators of epileptic activity: comparing entropic and hierarchical Bayesian approaches, PLoS One 8 (2) (2013) e55969.
[44] K. Friston, L. Harrison, J. Daunizeau, S. Kiebel, C. Phillips, N. Trujillo-Barreto, R. Henson, G. Flandin, J. Mattout, Multiple sparse priors for the M/EEG inverse problem, NeuroImage 39 (3) (2008) 1104–1120.
[45] R.N. Henson, H. Abdulrahman, G. Flandin, V. Litvak, Multimodal integration of M/EEG and f/MRI data in SPM12, Front. Neurosci. 13 (2019) 300.
[46] A.M. Dale, M.I. Sereno, Improved localization of cortical activity by combining EEG and MEG with MRI cortical surface reconstruction: A linear approach, J. Cogn. Neurosci. 5 (2) (1993) 162–176.
[47] J. Xu, J. Sheng, T. Qian, Y.-J. Luo, J.-H. Gao, EEG/MEG source imaging using fMRI informed time-variant constraints, Hum. Brain Mapp. 39 (4) (2018) 1700–1711.
[48] W.-T. Chang, A. Nummenmaa, J.-C. Hsieh, F.-H. Lin, Spatially sparse source cluster modeling by compressive neuromagnetic tomography, NeuroImage 53 (1) (2010) 146–160.
[49] R.A. Chowdhury, I. Merlet, G. Birot, E. Kobayashi, A. Nica, A. Biraben, F. Wendling, J.M. Lina, L. Albera, C. Grova, Complex patterns of spatially extended generators of epileptic activity: Comparison of source localization methods cMEM and 4-ExSo-MUSIC on high resolution EEG and MEG data, NeuroImage 143 (2016) 175–195.
[50] N. Level Otsu, A threshold selection method from gray-level histogram, IEEE Trans. Syst. Man Cybern. 9 (1) (1979) 62–66.
[51] C. Phillips, M.D. Rugg, K.J. Friston, Anatomically informed basis functions for eeg source localization: combining functional and anatomical constraints, NeuroImage 16 (2002) 678–695.
[52] V.D. Calhoun, J. Liu, T. Adali, A review of group ICA for fMRI data and ICA for joint inference of imaging, genetic, and ERP data, NeuroImage 45 (2009) S163–S172.
[53] S. Hassantabar, X. Dai, N.K. Jha, Steerage: Synthesis of neural networks using architecture search and grow-and-prune methods, arXiv preprint arXiv:1912.05831..
[54] S. Hassantabar, Z. Wang, N.K. Jha, Scann: Synthesis of compact and accurate neural networks, arXiv preprint arXiv:1904.09090..

Ke Liu received the B.S. degree in Automatic Control from Southwest University, Chongqing, China, in 2011. He received Ph.D. degree in pattern recognition and intelligent systems from South China University of Technology, Guangzhou, China, in 2016. He is currently an associate professor in College of Computer Science and Technology, Chongqing University of Posts and Telecommunications, Chongqing, China. His research interests include pattern recognition, Bayesian inference and their applications in EEG data analysis.

Zhu Liang Yu received his BSEE in 1995 and MSEE in 1998, both in electronic engineering from the Nanjing University of Aeronautics and Astronautics, China. He received his Ph. D. in 2006 from Nanyang Technological University, Singapore. He joined Center for Signal Processing, Nanyang Technological University from 2000 as a research engineer, then as a Group Leader from 2001. In 2008, he joined the College of Automation Science and Engineering, South China University of Technology and was promoted to be a full professor in 2010. His research interests include signal processing, machine learning and their applications in biomedical engineering, intelligent robotics etc.

Wei Wu received the Ph.D. degree in biomedical engineering from Tsinghua University, China, in 2012. From 2008 to 2010, he was a visiting student at the Neuroscience Statistics Laboratory, Department of Brain and Cognitive Sciences, Massachusetts Institute of Technology. Since 2012, he has been with the School of Automation Science and Engineering, South China University of Technology, as an associate professor. He was promoted to be a professor in 2020. He works in the field of neural signal processing and neural engineering, specializing in particular on developing statistical models and algorithms for the analysis and decoding of brain signals. He is an associate editor of Neurocomputing (Elsevier) and Neural Processing Letters (Springer), and a member of IEEE Biomedical Signal Processing Technical Committee. He is a senior member of the IEEE.

Chen Xun received the B.S. degree from the Department of Electronic Science and Technology, University of Science and Technology of China (USTC), in 2009, and the Ph.D. degree from the Department of Electrical and Computer Engineering, The University of British Columbia (UBC), in 2014. He is currently with the Hefei National Laboratory for Physical Sciences at the Microscale, Department of Electronic Science and Technology, USTC, as a Professor. His research interests include the broad areas of statistical signal processing and machine learning in biomedical applications.

Zhenghui Gu received the Ph.D. degree from Nanyang Technological University, Singapore, in 2003. From 2002 to 2008, she was with the Institute for Infocomm Research, Singapore. In 2008, she joined the College of Automation Science and Engineering, South China University of Technology, Guangzhou, as an associate professor. She was promoted to be a full professor in 2015. Her current research interests include the fields of signal processing and pattern recognition.

Cuntai Guan (Fellow, IEEE) received the Ph.D. degree in electrical and electronic engineering from Southeast University, Nanjing, China, in 1993. He is currently a Professor with the School of Computer Science and Engineering, Nanyang Technological University, Singapore. His research interests include brain-computer interfaces, neural signal processing, neural image processing, machine learning, and artificial intelligence. Dr. Guan received the Annual BCI Research Award, the IES Prestigious Engineering Achievement Award, the Achiever of the Year (Research) Award, and the Finalist of President Technology Award. He is an Associate Editor of the IEEE TRANSACTIONS ON BIOMEDICAL ENGINEERING, Pattern Recognition, Neurocomputing, Frontiers in Human Neuroscience, and Brain-Computer Interfaces.